OKLAHOMA TRANSPORTATION CENTER

ECONOMIC ENHANCEMENT THROUGH INFRASTRUCTURE STEWARDSHIP

INNOVATIVE PREDICTION OF FLY ASH PERFORMANCE IN CONCRETE

MOHAMMED ABOUSTAIT
QINANG HU
ROBERT FRAZIER
YANLI ZHANG
BRADEN TABB
TYLER LEY, PH.D., P.E.
JAY HANNA, PH.D.

OTCREOS10.1-25-F

Oklahoma Transportation Center
2601 Liberty Parkway, Suite 110
Midwest City, Oklahoma 73110

Phone: 405.732.6580
Fax: 405.732.6586
www.oktc.org

DISCLAIMER

The contents of this report reflect the views of the authors, who are responsible for the facts and accuracy of the information presented herein. This document is disseminated under the sponsorship of the Department of Transportation University Transportation Centers Program, in the interest of information exchange. The U.S. Government assumes no liability for the contents or use thereof.

TECHNICAL REPORT DOCUMENTATION PAGE

1. Report No.	2. Government Accession No.	3. Recipient's Catalog No.	
OTCREOS10.1-25-F			
4. Title and Subtitle Innovative Prediction of Fly Ash Performance in Concrete		**5. Report Date** February 2013 **6. Performing Organization Code**	
7. Author(s) Mohammed Aboustait, Qinang Hu, Robert Frazier, Yanli Zhang, Braden Tabb, Tyler Ley, and Jay Hanan		**8. Performing Organization Report No.**	
9. Performing Organization Name and Address Oklahoma State University School of Civil and Environmental Engineering 207 Engineering South Stillwater, OK 74078		**10. Work Unit No. (TRAIS)** **11. Contract or Grant No.** DTRT06-G-0016	
12. Sponsoring Organization Name and Address Oklahoma Transportation Center (Fiscal) 201 ATRC Stillwater, OK 74078 (Technical) 2601 Liberty Parkway, Suite 110 Midwest City, Oklahoma 73110		**13. Type of Report and Period Covered** Final February 2010 – February 2013 **14. Sponsoring Agency Code**	
15. Supplementary Notes Project performed in cooperation with the Oklahoma Transportation Center and the University Transportation Center Program			

16. Abstract

In the last half century much research has been conducted to find an acceptable cement substitute; the most intriguing and interesting of those materials is fly ash. Fly ash consists of almost perfectly spherical particles that are rich in calcium, silicon, iron and aluminum.

The report outlines preliminary work on several novel particle analysis techniques used to investigate fly ash. Also included is a series of physical tests used to investigate the strength, performance in alkali silica reaction, and chloride penetration of fly ash. Although more work is needed to make strong findings, the particle analysis techniques were able to find differences in these materials when bulk analysis could not. These findings are critical to better elucidating the difference in performance in these materials.

17. Key Words	18. Distribution Statement		
Microanalysis, mCT, Automated SEM, fly ash, TACCo	No restrictions. This publication is available at www.oktc.org and from the NTIS.		
19. Security Classification (of this report)	**20. Security Classification (of this page)**	**21. No. of Pages**	**22. Price**
Unclassified.	Unclassified.	78 + covers	

SI (METRIC) CONVERSION FACTORS

Approximate Conversions to SI Units

Symbol	When you know	Multiply by	To Find	Symbol
	LENGTH			
in	inches	25.40	millimeters	mm
ft	feet	0.3048	meters	m
yd	yards	0.9144	meters	m
mi	miles	1.609	kilometers	km
	AREA			
in^2	square inches	645.2	square millimeters	mm
ft^2	square feet	0.0929	square meters	m^2
yd^2	square yards	0.8361	square meters	m^2
ac	acres	0.4047	hectares	ha
mi^2	square miles	2.590	square kilometers	km^2
	VOLUME			
fl oz	fluid ounces	29.57	milliliters	mL
gal	gallons	3.785	liters	L
ft^3	cubic feet	0.0283	cubic meters	m^3
yd^3	cubic yards	0.7645	cubic meters	m^3
	MASS			
oz	ounces	28.35	grams	g
lb	pounds	0.4536	kilograms	kg
T	short tons (2000 lb)	0.907	megagrams	Mg
	TEMPERATURE (exact)			
°F	degrees Fahrenheit	(°F-32)/1.8	degrees Celsius	°C
	FORCE and PRESSURE or STRESS			
lbf	poundforce	4.448	Newtons	N
lbf/in^2	poundforce per square inch	6.895	kilopascals	kPa

Approximate Conversions from SI Units

Symbol	When you know	Multiply by	To Find	Symbol
	LENGTH			
mm	millimeters	0.0394	inches	in
m	meters	3.281	feet	ft
m	meters	1.094	yards	yd
km	kilometers	0.6214	miles	mi
	AREA			
mm^2	square millimeters	0.00155	square inches	in^2
m^2	square meters	10.764	square feet	ft^2
m^2	square meters	1.196	square yards	yd^2
ha	hectares	2.471	acres	ac
km^2	square kilometers	0.3861	square miles	mi^2
	VOLUME			
mL	milliliters	0.0338	fluid ounces	fl oz
L	liters	0.2642	gallons	gal
m^3	cubic meters	35.315	cubic feet	ft^3
m^3	cubic meters	1.308	cubic yards	yd^3
	MASS			
g	grams	0.0353	ounces	oz
kg	kilograms	2.205	pounds	lb
Mg	megagrams	1.1023	short tons (2000 lb)	T
	TEMPERATURE (exact)			
°C	degrees Celsius	9/5+32	degrees Fahrenheit	°F
	FORCE and PRESSURE or STRESS			
N	Newtons	0.2248	poundforce	lbf
kPa	kilopascals	0.1450	poundforce per square inch	lbf/in^2

ACKNOWLEDGMENTS

A massive acknowledgement should be given to Jeff Davis of the Surface Chemistry and Microanalysis group at NIST for help with the electron microprobe and the automated SEM work in this report. Without his help this work would not have been completed.

We would also like to thank the Oklahoma Transportation Center for funding this work and the purchase of several key pieces of equipment through an equipment grant competition.

INNOVATIVE PREDICTION OF FLYASH PERFORMANCE IN CONCRETE

Final Report: February, 2013

Mohammed Aboustait
Qinang Hu
Robert Frazier
Yanli Zhang
Braden Tabb
Tyler Ley, Ph.D., P.E.
Jay Hanan, Ph.D.

Oklahoma State University
Civil and Environmental Engineering Department
207 Engineering South
Stillwater, OK 74078

TABLE OF CONTENTS

Chapter 1 - Introduction *1*

Fly Ash 1

Chapter 2 - Use of an Automated SEM to Investigate Fly Ash *4*

Scanning Electron Microscope 4

Automated Feature Analysis 6

Use of the AFA-SEM to investigate Fly Ash 7

Sample Preparation 7

SEM Calibration and EDS Settings 8

SEM Imaging Settings 11

SEM-AFA Consistency 14

Morphological Comparison 22

Chemical Comparison 25

Future work 30

Armstrong Correction 30

Clustering 30

Combination with physical testing results 30

Summary 31

Chapter 3 - Use of Micro Tomography to Investigate Fly Ash *32*

Methods 34

Sample Description and Preparation 35

Micro Computed Tomography 36

Electron Probe Microanalysis 38

Fusing Electron Probe Microanalysis and micro Computed Tomography Datasets 39

Segmentation of the micro Computed Tomography Data 40

Results 42

Micro-Computed Tomography 42

Electron Probe Microanalysis 42

Data Fusion 44

3D Data Analysis 47

Discussion **47**
Repeatability of the Method **48**
Compositional Makeup of Fly Ash **48**
Chemical Consistency with Depth **48**
Summary **49**
Chapter 4 - Physical Testing ***51***
Fresh concrete testing **53**
Harden concrete testing **54**
ASTM C39 - Compressive Strength **54**
ASTM C1556 - **56**
ASTM C1293 – **59**
Summary **62**
Chapter 5 – Conclusion ***64***
REFERENCES ***65***

List of Figures

FIGURE 1: AN IMAGE OF THE ASPEX EXPLORER PSEM SYSTEM INSTALLED AT THE MICROSCOPY CENTER AT OSU – STILLWATER, OKLAHOMA 4
FIGURE 2: AN ILLUSTRATION SHOWING THE OUTCOME OF AN ELECTRON BEAM HITTING A SOLID SURFACE 5
FIGURE 3: A TYPICAL SE IMAGE OF A FLY ASH PARTICLE 5
FIGURE 4: A TYPICAL BS IMAGE OF A FLY ASH PARTICLE 6
FIGURE 5: AN IMAGE OF TYPICAL EDS SPECTRUM. 6
FIGURE 6: AN ILLUSTRATION OF THE SEM-AFA SCAN PROCEDURE 7
FIGURE 7: AN IMAGE OF TYPICAL SEM ALUMINUM STUB COVERED WITH DOUBLE ADHESIVE CARBON TAPE 8
FIGURE 8 & 9: TWO IMAGES OF THE SAME MASS OF FLY ASH PARTICLES. 11
FIGURE 10: THE THRESHOLD VALUES APPLIED ON AN INDIVIDUAL FLY ASH PARTICLE. GREEN COLOR REPRESENTS MEASUREMENT RANGE WHILE YELLOW COLOR REPRESENTS DETECTION RANGE. 13
FIGURE 11: AN ILLUSTRATION OF THE SCANNED AREA ON THE SEM COUPLED WITH SE IMAGE OF THE SAME AREA 14
FIGURE 12: DIAMETER COMPARISON FOR THREE SCANS OF THE SAME FLY ASH SAMPLE. ERROR BARS WITH ONE STANDARD DEVIATION ARE SHOWN. 15
FIGURE 13: AREA COMPARISON FOR THREE SCANS OF THE SAME FLY ASH SAMPLE. ERROR BARS WITH ONE STANDARD DEVIATION ARE SHOWN. 16
FIGURE 14: PERIMETER COMPARISON FOR THREE SCANS OF THE SAME FLY ASH SAMPLE. ERROR BARS WITH ONE STANDARD DEVIATION ARE SHOWN. 16
FIGURE 15: THREE BS IMAGES FOR THE SAME FLY ASH PARTICLE, EACH OF THE IMAGES HAVE BEEN COLLECTED FROM ONE OF THE THREE SCANS CONDUCTED. 17
FIGURE 16: A LINE SCAN COMPARISON BETWEEN THE THREE BS IMAGES FOR THE SAME FLY ASH PARTICLE 17
FIGURE 17: LIVE TIME PER PARTICLE COMPARISON FROM THREE DIFFERENT SCANS. 18
FIGURE 19: THE RELATION BETWEEN LIVE TIME AND X-RAY COUNTS PER PARTICLE. 19
FIGURE 20: DIAMETER VS FREQUENCY FOR PARTICLES SMALLER THAN 75 MICRONS 22
FIGURE 21: DIAMETER VS FREQUENCY FOR C3 FLY ASH FOR THE THREE MOST DOMINANT ELEMENTS 23
FIGURE 22: BS IMAGE FOR THE SI RICH FLY ASH PARTICLES. 25
FIGURE 23: BS IMAGE FOR THE AL RICH FLY ASH PARTICLES 25
FIGURE 24: BS IMAGE FOR THE CA RICH FLY ASH PARTICLES. 26
FIGURE 25: A COMPARISON BETWEEN A TYPICAL SI RICH PARTICLE, AL RICH PARTICLE AND CA RICH PARTICLE 26
FIGURE 26: MAJOR ELEMENTS CORRESPONDING TO THE HIGHEST NO. OF COUNTS DETECTED IN THE AFA SCANS 27
FIGURE 27: BULK XRF FOR MAJOR ELEMENTS 28
FIGURE 28: MINOR ELEMENTS CORRESPONDING TO THE HIGHEST NO. OF COUNTS DETECTED IN THE AFA SCAN 29
FIGURE 29: BULK XRF FOR MINOR ELEMENTS 29
FIGURE 30: AN OVERVIEW OF THE PROCESSES USED FOR FUSING THE EPMA AND μCT DATA SETS. 34
FIGURE 31: THE NUMBER OF VOXELS AT DIFFERENT GRAY SCALE VALUES FROM THE 3D □CT DATA SET FOR PARTICLE 1C. 37

FIGURE 32: THE GRAY SCALE IMAGES SHOWS THE BACKSCATTER AND ELEMENTAL MAPS FROM EPMA FOR PARTICLE 1C. THE SEGMENTED CONSTITUENT PHASE ANALYSIS USED IN TACCO IS SHOWN IN THE UPPER RIGHT. 39
FIGURE 33: A 3D MODEL OF THE SEGMENTED μCT DATA. ONE QUADRANT OF THE MATERIAL HAS BEEN REMOVED SO THAT IT IS EASIER TO VIEW THE DISTRIBUTION OF CONSTITUENTS WITHIN THE PARTICLE. 41
FIGURE 34: SHELLS OR LAYERS WITH 1 μM UNIFORM THICKNESS PARALLEL TO THE PARTICLE SURFACE WERE ANALYTICALLY PEELED FROM EXTERIOR SURFACE AT DIFFERENT DEPTHS. 42
FIGURE 35:A TERNARY DIAGRAM FOR THE SI, CA AND AL COMPOSITION FOR DIFFERENT UNIQUE CONSTITUENTS. 44
FIGURE 36: A COMPARISON OF THE EPMA AND μCT DATA. THE TOP PLOT SHOWS THE NUMBER OF PIXELS VERSUS THE GRAY SCALE VALUE FROM THE DATA SETS. THE MEAN IS SHOWN AS A SOLID LINE AND THE STANDARD DEVIATION AS A DASHED LINE. THE BOTTOM PLOT SHOWS THE NUMBER OF VOXELS VERSUS GRAY SCALE FOR THE ENTIRE PARTICLE WITH THE PROJECTED MEAN AND STANDARD DEVIATIONS 45
FIGURE 37 – SUMMARY OF SEGMENTATION RANGES FOR THREE PARTICLES. 46
FIGURE 38: A PLOT OF THE PERCENTAGE OF EACH OF THE SEGMENTED PHASES WITHIN THE 3D PARTICLE VERSUS THE DISTANCE FROM THE CENTROID OF THE PARTICLE. 47
FIGURE 39: THE RELATIONSHIP BETWEEN COMPRESSIVE STRENGTH AND THE TYPE OF FLY ASH OVER THE FIRST 28 DAYS. 54
FIGURE 40: THE RELATIONSHIP BETWEEN THE COMPRESSIVE STRENGTH AND THE TYPE OF FLY ASH. 55
FIGURE 41: PROFILE GRINDING USING A DRILL PRESS WITH 1 INCH CORE BIT 56
FIGURE 42: THE CHLORIDE PROFILE VERSUS DEPTH AT 45 DAYS. 57
FIGURE 43: THE CHLORIDE PROFILE VERSUS DEPTH AT 90 DAYS. 58
FIGURE 44: THE CHLORIDE PROFILE VERSUS DEPTH AT 135 DAYS. 58
FIGURE 45: SHOWS THE ASR EXPANSION VS TIME 61
FIGURE 46: THE WEIGHT CHANGE VS TIME FOR THE ASTM C 1293 SPECIMENS. 62

List of Tables

TABLE 1 - CHEMICAL COMPOSITION FROM BULK XRF OF 5 COMMERCIAL FLY ASHES ADOPTED. 2
TABLE 2 - SUMMARY OF INSTRUMENT CALIBRATION AND EDS SETTING 10
TABLE 3 - THE ELEMENTS THAT FORM THE CHEMICAL MAKEUP OF FLY ASH 10
TABLE 4–SEM AFA IMAGING SETTINGS 12
TABLE 5- A SUMMARY OF THE IMAGE THRESHOLD VALUES USED DURING A TYPICAL AFA SCAN FOR FLY ASH PARTICLES 14
TABLE 6 -THE HIGHEST ELEMENT AND THE CORRESPONDING NO. OF COUNTS PER PARTICLE FOR ALL THREE SCANS 19
TABLE 7 -THE AVERAGE DIAMETER FOR THE 5 COMMERCIAL TYPES OF FLY ASH 23
TABLE 8 - MAXIMUM-IN-FREQUENCY DIAMETER FOR THE 5 COMMERCIAL TYPES OF FLY ASH 24
TABLE 9 -DIAMETER RANGE VS AVERAGE ASPECT RATIO (AAR) FOR THE 5 COMMERCIAL TYPES OF FLY ASH 25
TABLE 10 – A POWDER XRF ANALYSIS FOR THE FLY ASH INVESTIGATED IN THIS STUDY 35
TABLE 11 – SCAN SETTINGS FROM THE µCT. 37
TABLE 12 – SUMMARY OF THE DIFFERENT COMPOSITIONS OBSERVED WITH THE EPMA. 43
TABLE 13 –SUMMARY OF THE MEAN AND STANDARD DEVIATIONS OF ALL THE PHASES. 46
TABLE 14 - CHEMICAL COMPOSITION OF THE CEMENT ADOPTED 52
TABLE 15 - MIX PROPORTION USED IN ASTM C39 & C1556 53
TABLE 16 - MIX PROPORTION USED IN ASTM C1293 53
TABLE 17 - FRESH CONCRETE PROPERTIES 53
TABLE 18 - THE ALKALI CONTENT AND CA/SI FOR THE FIVE COMMERCIAL TYPES OF FLY ASH 61
TABLE 19–SUMMARY FOR THE OVERALL PERFORMANCE AND PERCENT DIFFERENCE OF ALL HARDEN PHYSICAL TESTING NORMALIZED WITH RESPECT TO THE CONTROL MIXTURE . 63

Executive Summary

Fly ash is a waste product gathered from the emissions of coal fired power plants. It is estimated that the worldwide production of fly ash is over 750 million metric tons. Currently only 40% of this material is used in other processes and the other material is placed in special landfills.

Fly ash is made up of crystalline and amorphous phases containing predominantly Al, Si, Ca and Fe. The particles are generally spherical with diameters ranging from less than 1 μm to more than 1 mm. Fly ash is commonly used as a low cost construction binder for stabilization of soil, a partial replacement of portland cement in a concrete mixture, and the predominate binder in a geopolymer concrete.

Despite the widespread use of this material, there are still a number of important unanswered questions. Past research has also shown that fly ash in concrete mixtures has the ability to improve the strength, reduce the permeability, and improve the rheology of fresh concrete mixtures, as well as provide resistance to a number of common durability problems. Depending on the properties of the fly ash, it can either act as a supplementary binder or take part in a secondary pozzolanic reaction with the alkaline pore solution and calcium hydroxide. Substitution levels for portland cement in a concrete mixture are commonly limited to 20% by mass. This limit is imposed because fly ash is not a manufactured material and therefore not all sources have the same performance in concrete. If this material was better understood then the usage levels could be increased.

This report outlines the use of two different novel particle analysis techniques applied to fly ash. This was done for six different fly ash sources. In addition, testing was done to examine the performance of these fly ashes in concrete mixtures. The novel particle analysis techniques were shown to be capable of finding significant differences in the particle chemistry and size distribution when the bulk methods could not.

This work is helpful to better understand the chemical makeup and characteristics of fly ash particles and how these impact their performance in concrete. While no strong findings can be drawn from this initial work, these efforts have allowed additional funding to be obtained to continue these investigations.

CHAPTER 1 - INTRODUCTION

In the last half century much research has been conducted to find an acceptable cement substitute; the most intriguing and interesting of those materials is fly ash. Fly ash consists of almost perfectly spherical particles that are rich in calcium, silicon, iron, and aluminum.

Through this work the authors are exploring a reliable and practical methodology for better understanding fly ash through a mixture of testing sets varying between typical physical experimental techniques and cutting edge characterization techniques at a number of length scales. The most renowned of these cutting edge techniques was investigating single fly ash particles with Scanning Electron Microscope and Micro Computed Tomography. Upon conducting such techniques on a variety of fly ashes coupled with conducting the standardized ASTM testing, such as compression testing (ASTM C39), alkali-silica reaction (ASTM C1293), and bulk chloride diffusion (ASTM C1556), the expected outcome will offer new insights into the performance of fly ash within concrete.

Fly Ash

Fly ash, which has come to be known as the “fourth ingredient” in the concrete industry[1], has shown tremendous demand for the past decade due to its ability to make so many different improvements to the performance of concrete.

Fly ash is widely known for its usage in the concrete industry as supplementary cementitious material capable of enhancing some of the concrete properties over time. However, it also has been used as filler and reinforcement material in several other industries such as soil stabilization, landfilling, geopolymers, ceramics, and many other composite materials[2-3]. Fly ash is the product of combustion of pulverized coal in power plants. After the burning procedure is completed, the fly ash is collected before escaping into the air by means of a number of methods, the most common of which is the electrostatic collector.

In ASTM C618 fly ash particles are classified as either class C or F. Class C is produced from burning sub-bituminous coal and usually exhibits self-cementing properties, while class F is produced from burning the harder, older bituminous coal. Class F fly ash usually needs to react with lime and alkalis within the cement in order to form cementitious compound [4].

While there is no mention of the calcium content in the specifications, it is widely recognized that class C fly ash has high calcium oxide content and class F fly ash has lower calcium oxide content.

Table 1 summarizes the elemental oxides from bulk XRF detected in five different commercial types of fly ash considered within this study. Three of these fly ashes are classified as C, one is F, and the last is C/F according to ASTM C618 specifications.

Table 1 - Chemical composition from bulk XRF of 5 commercial fly ashes adopted.

Fly Ash	C1	F	C2	C3	C/F
SiO_2 (%)	39.13	56.72	36.21	38.34	38.13
Al_2O_3 (%)	20.37	20.29	19.94	19.87	20.99
Fe_2O_3 (%)	6.15	5.62	6.67	6.12	5.46
CaO (%)	21.18	9.95	23.96	23.07	15.54
MgO (%)	5.33	2.97	5.17	5.16	3.71
Na_2O (%)	1.60	0.54	1.67	1.53	7.88
K_2O (%)	0.65	1.38	0.52	0.62	0.77
TiO_2 (%)	1.33	1.12	1.44	1.43	1.31
MnO_2 (%)	0.02	0.09	0.03	0.02	0.04
P_2O_5 (%)	1.60	0.13	1.44	1.09	0.67
SrO (%)	0.34	0.27	0.38	0.35	0.72
BaO (%)	0.72	0.26	0.69	0.64	1.47
SO_3 (%)	1.37	0.51	1.44	1.14	2.90
L.O.I (%)	0.24	0.16	0.15	0.62	0.41
Moisture (%)	0.11	0.02	0.04	0.01	0.03

It can be observed from Table 1 that the loss on ignition (L.O.I), which is an indication of unburned carbon within fly ash particles, was relatively very low among all five commercial types of fly ashes compared to the ASTM C618 specification maximum limit of 6%. By comparing the accumulated major oxides in Table 1, it can be observed that C1, C2 and C3 are very similar in their chemical composition, while F and C/F have a very distinct composition from each other and the rest of C fly ashes. However, despite the similarity between the class C fly ashes there is a slight difference in silicon content between C2 and the other two class C ashes, C1 and C3; similarly there is a difference in calcium content between C1 and the other two ashes, C2 and C3. By comparing the major oxides detected in each of the 5 commercial types of fly ash it can

be observed that all class C fly ashes had higher iron, sulfate and alkali contents than class F, but class F ashes had higher potassium content than class C ashes. Also, class F, where the silicon content exceeded half of its total content, had very high silicon content compared to both classes C and C/F. However, C/F had silicon content identical to C1 and C3, iron content identical to F, and calcium content not as high as the C ashes and not as low as the F ash. The uniqueness of C/F can be observed in its sodium and sulfate content, 7.88% and 2.90% respectively; such high values enabled this type of fly ash to perform differently, as illustrated later on in this report. All the 5 fly ashes were found to be very similar in their aluminum content.

As seen in the previous Table, Table 3, the values for any of the three C fly ashes or even the other two ashes in any of the mentioned criteria can vary enormously, as in fact those criteria are highly dependent on the coal source, coal type, power plant burning and ash collecting procedure.

The chemical and physical properties of fly ash always have been a major interest for researchers [5-8.] The physical properties of the concrete mixtures containing the embedded fly ashes will be examined by conducting an SEM-AFA scan as well as a set of standardized ASTM tests on the five commercial types of fly ash.

CHAPTER 2 - USE OF AN AUTOMATED SEM TO INVESTIGATE FLY ASH

This chapter summarizes an ongoing microscopy study of fly ash. The use of scanning electron microscopes (SEMs) equipped with an energy dispersive x-ray spectrometer (EDS) offers a useful technique to quantify the complex micro-structure and chemistry of materials of fly ash. Recent advances in Automated Feature Analysis (AFA) of SEMs have made them a very powerful analytical tool, as the analysis can be completed automatically while the instrument is not operated by a human. This is the first report in the known literature to investigate individual fly ash particles with this automated technique.

Scanning Electron Microscope

The ASPEX SEM was obtained through an equipment grant from the OkTC and is shown in Figure 1. This system provides a scanning electron microscope with a built-in energy dispersive x-ray spectrometer that is able to create elemental maps of the surface with a minimum scale of 250 nm.

Figure 1: An image of the ASPEX Explorer PSEM system installed at the Microscopy Center at OSU – Stillwater, Oklahoma

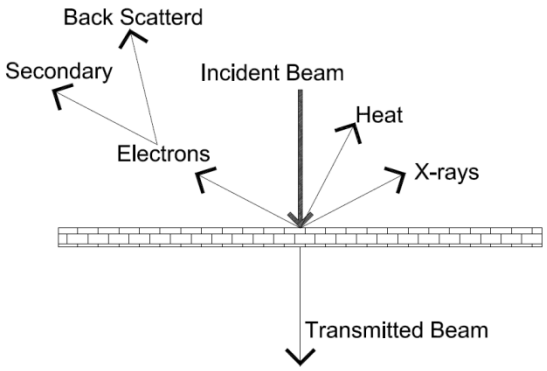

Figure 2: An illustration showing the outcome of an electron beam hitting a solid surface

The SEM uses a focused electron beam generated from the tungsten filament through a nickel column to scan the surface of a sample under vacuum conditions. During this scan, the electron beam enters the specimen through a nickel column, and a variety of signals in the form of electrons and x-rays are ejected as seen Figure 2[9]. These signals are then collected by different detectors. This SEM uses the backscattered electron detector (BSD) to capture the primary electrons, the secondary electron detector (SED) to capture low energy electrons, and the EDS detector to capture the x-rays. The SED is used to obtain topographic and fine detail information at low accelerating voltages, as seen in Figure 3, while BSD is used to obtain grey level compositional information from the sample. Using the BSD, materials with different electron density or average atomic number appear differently, as seen in Figure 4.

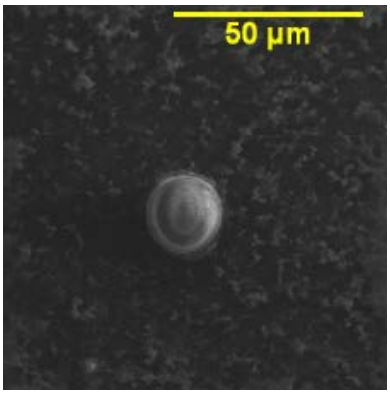

Figure 3: A typical SE image of a fly ash particle

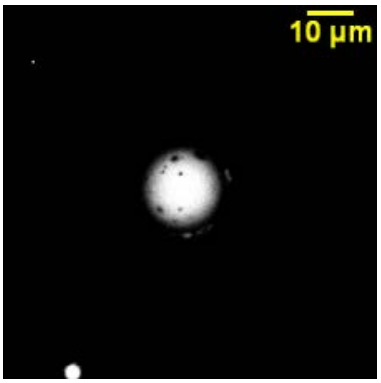

Figure 4: A typical BS image of a fly ash particle

The EDS detector collects the repelled x-rays generated by the interaction of electrons with the excited depth of scanned material to offer a chemical composition in the form of x-ray spectrum, as seen in Figure 5[9-12]. This spectrum is made of peaks representing characteristic x-rays emitted by the different elements in the scanned material. The characteristic x-rays have fixed energies determined by the energy difference between the electron shells.

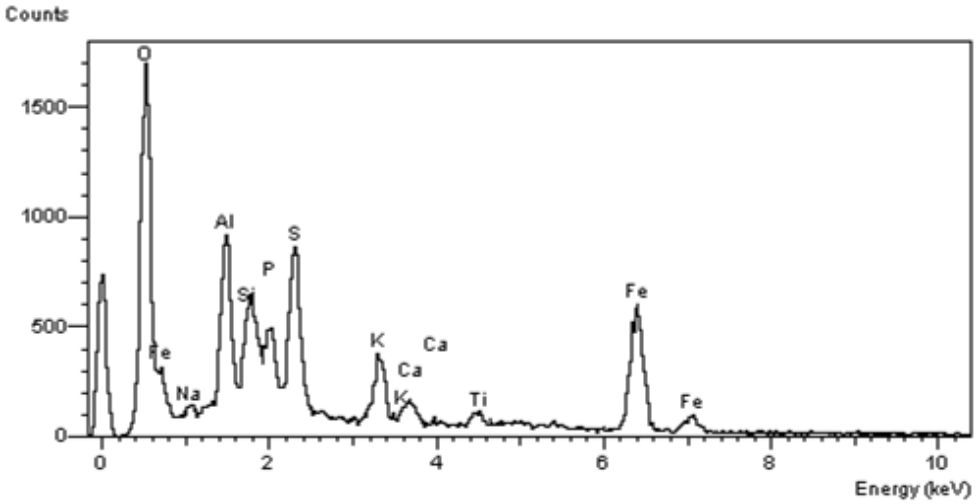

Figure 5: An image of typical EDS spectrum.

Automated Feature Analysis

The automated feature analysis (AFA) is a scanning option within the SEM which enables the survey of thousands of fly ash particles in a timely manner. The scanning procedure starts by defining a region of interest on an SEM stub, as outlined in Figure 6. This region is divided into equal rectangles by the SEM, known as fields. Each field is inspected by the electron beam as it goes through inspecting for particles in a chord

searching pattern with a format starting from left to right. Any material found along these chord formats gets recorded as long it satisfies the imaging settings installed prior to the scan. This inspection is followed by enlisting each of the particles detected into elemental based criteria checks in which the chemical composition of each individual particle is investigated; these criteria are similarly defined prior to the scan taking place. These criteria checks are based on an input file specifying the typical element instituted within fly ash as material in addition to specifying the minimum counts required to be collected per particle. These files act as a check list that are used to filter the data through defining which of the particles will get accepted, counted and analyzed, and which will not. The output from this procedure is robust data including both morphological data and elemental constituents for each of the examined particles satisfying imaging settings and criteria checks.

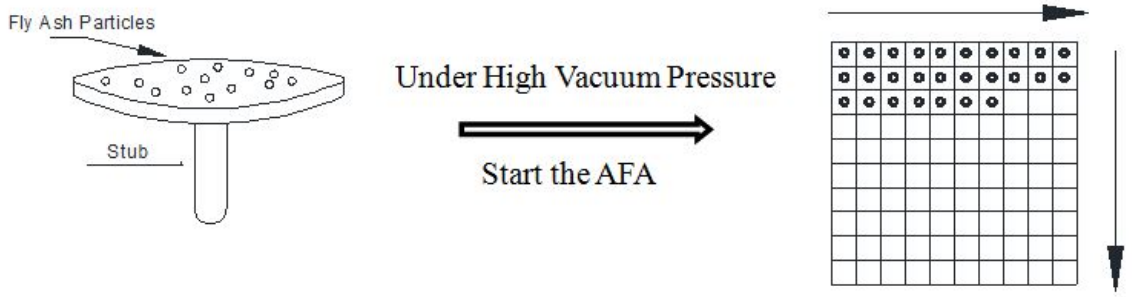

Figure 6: An illustration of the SEM-AFA scan procedure

Use of the AFA-SEM to investigate Fly Ash

In general, the repeatability and accuracy of any AFA-SEM scan is limited to sample preparation, calibration standards, EDS settings, imaging settings, instrumental errors, and statistics. Therefore, defining each of these parameters plays an integral role in achieving the optimum qualitative and quantitative data requested from the AFA scanning option. Each of these parameters will be explained in detail, elaborating on the scanning procedure and methodology.

Sample Preparation

Using the automated capabilities of SEM to investigate fly ash is conducted through a simple procedure of mounting well dispersed fly ash particles on a carbon adhesive surface capable of maintaining these particles in place and set for scanning. The sample preparation procedure can be defined in the following steps:

- Initially, fly ash must be sieved to 75 micron diameter and less using a normal sieve shaker and the ash passing through sieve #200 is collected.
- This is followed by preparing an equal proportion solution of isopropyl alcohol and acetone at a mixing ratio of 1:1 (25 ml acetone + 25 ml isopropyl = 50 ml overall), this mixture acts as a fast-evaporating solvent in which the fly ash will be ultrasonicated and held in suspension.
- Then take a 0.0100 g sample of fly ash and add to the solution. The output should be sonicated for 30 minutes to ensure a good dispersion of fly ash particles within the solution.
- Make sure the SEM sample holder is clean, and then attach a double side adhesive carbon tape to it. Peel the cover of the double sided tape while wearing clean gloves and avoid touching the surface of the carbon tape.
- Using a precise pipette, place a small drop of the fly ash solution on the carbon tape and allow the solution to evaporate under a heated lamp. The final product can be seen in Figure 7.
- Next place the stub in a vacuum until testing.

Figure 7: An image of typical SEM aluminum stub covered with double adhesive carbon tape

SEM Calibration and EDS Settings

It was first important to establish the correct instrument settings for the SEM in order to achieve a reliable EDS setting. This was done through collaborative work with Jeff Davis of NIST. Defining the EDS scan settings was necessary in order to identify the running beam current, spot size, and probe current required to excite the different elements within fly ash particles as well as to achieve a satisfactory x-ray count rate from it. The running beam current is the current that leaves the SEM electron gun, while the probe current is the current that reaches the specimen. The beam stability of the probe current is typically investigated with a faraday cup and pico-amp meter. The use

of a faraday cup is helpful as it determines the current under conditions as close as possible to those during data scanning collection.

The running beam current and its correlated probe current performance are solely dependent on the potential difference used to accelerate the SEM electron gun, simply known as the accelerating voltage*.* During the process of this research, all work with the SEM was done while the filament was saturated by setting the accelerating voltage to 20 KV for at least 30 minutes prior to work. It was determined to use such an accelerating voltage so that at least 1 nA of probe current is collected. This adopted voltage of 20 KV had successfully excited the elements typically found in fly ash, as seen in Table 2. The highest energy K-alpha line for a major element in fly ash is Iron at 6.38 KV; as a result a traditional overvoltage ratio of 2.5 to 3 was preserved do to the embracement of 20 KV as accelerating voltage. Table 2 outlines the instrument calibration values and EDS settings in addition to the results of investigating different size fly ash particles.

It should be mentioned that a complete characteristic x-ray spectrum is captured for each particle during the AFA-SEM scan, but in order for the evaluation process to be simplified for the user and shortened in processing time for the SEM machine, an input file was provided containing the typical elements observed within fly ash, as seen in Table 3[10,13-19]. These files, as mentioned earlier, act as check list that are used to filter the data in order to exclude any non-fly ash particles. This was coupled with requesting the minimum counts required for each real fly ash particle by specifying such a requirement within the same input file. The minimum x-ray count rate required from the different size fly ash particles was satisfied by adjusting the spot size to 45% as described in Table 2. Finally the image settings were adjusted in order to obtain satisfactory images at the accelerating voltage, probe current and spot size already defined and used in the EDS settings.

Table 2 - Summary of instrument calibration and EDS setting

	OSU	**NIST**
Spot Size	≈ 45%	
Accelerating Voltage	20 KV	20 KV
Filament Drive	75%	
Running Current	≈ 55 μA	
Pico-amp meter Reading	1.4 nA	≈ 1 nA
Copper Standard	13500 cps	10000 → 20000 cps
FLY ASH	Counts Per Second	Counts Per Second
Particle1 (1> μm)	6350	≈ 5000
Particle 2 (1 μm)	5900	≈ 5000
Particle 3 (≤ 1 μm)	5800	≈ 5000

Table 3 - The elements that form the chemical makeup of fly ash

Element	Symbol	Z (Atomic No.)
Oxygen	O	8
Sodium	Na	11
Magnesium	Mg	12
Aluminum	Al	13
Silicon	Si	14
Phosphorus	P	15
Sulfur	S	16
Potassium	K	19
Calcium	Ca	20
Titanium	Ti	22
Iron	Fe	26
Strontium	Sr	38
Zirconium	Zr	40

SEM Imaging Settings

SEM imaging settings are the settings through which a good spatial resolution of the collected images is achieved. The settings were selected to optimize the quality of image produced from each SEM-AFA scan. Upon verifying the accelerating voltage, probe current and spot size in the EDS settings, other factors such as brightness, contrast, and working distance had to be adjusted in order to obtain good quality images with EDS settings preserved. In order to make these adjustments, there needed to be enough signal from each fly ash particle so that it could be identified in the scan. The effect of such factors can be observed on Figures 8 and 9. These images have been captured by two different modes of imaging; figure 8 was captured by the secondary electron detector (SE), while figure 9 was captured by the backscattered electron detector (BS). After applying these settings on SE image, the quality of attained BS image was tremendously enhanced for both solid spheres and hollow cenospheres fly ashes. The carbon tape offered a good contrast to detect the border of the fly ash particles.

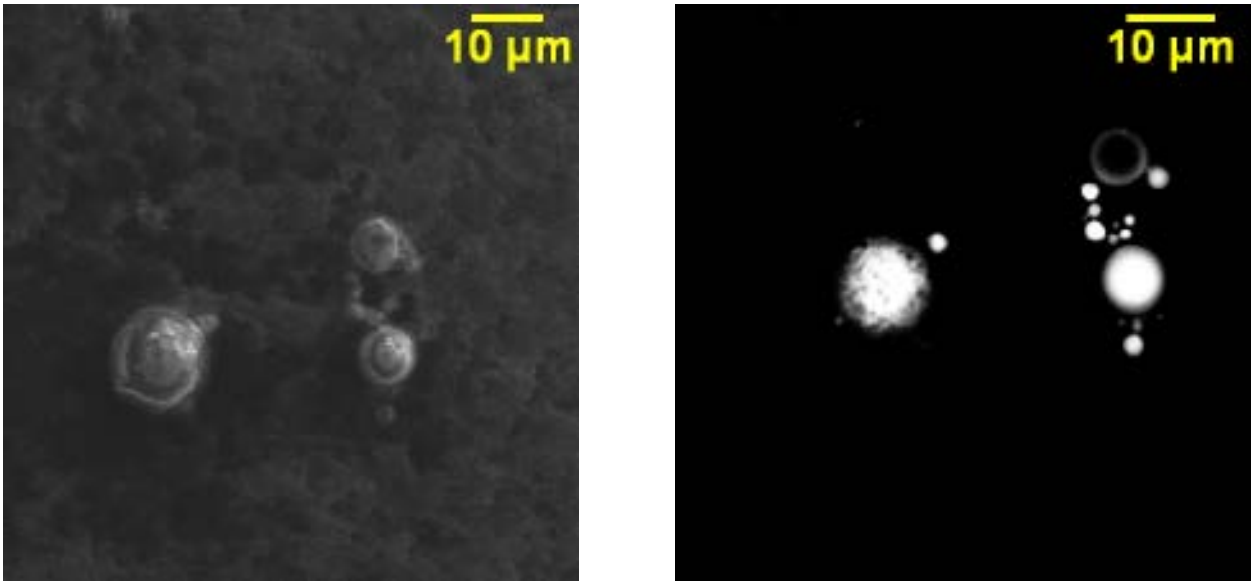

Figure 8 & 9: Two images of the same mass of fly ash particles.

On the left SE image, the particles borders are difficultly detected; however, after applying the recommended imaging settings, particles became more obvious with clearly defined borders in the BS image.

At an instrument magnification of 2500x, particles with diameters between0.1 to 40.5 µm can be detected. Fly ash particles are typically spherical in shape; through preliminary work it was determined that a detection aspect ratio shall be adopted in order to assist in detecting fly ash particles only. Aspect ratio is the ratio between the major axis of the fly particle to its minor axis. For a perfect circle, the aspect ratio is

1, through trial and error an aspect ratio of 1.3 was found to be a good parameter that led to only fly ash particles being detected. Table 4 contains a summary of the SEM imaging and scan settings.

Table 4–SEM AFA Imaging Settings

Detector	BSD
Brightness	- 30 %
Contrast	100 %
Working Distance	≈ 17.5 mm
Aspect Ratio	≤ 1.3
Particle Diameter Investigated	0.1 to 40.5 µm
Search Grid Dimensions	264 µm x 264 µm
Search Dwell Time	32 µsecond
Measure Dwell Time	64 µsecond

The dwell time is the time spent per pixel by the BSD detecting a particle, collecting its image and processing its morphological data for any given point throughout the scan. If the dwell time is not long enough, smaller particles might be over looked during the searching procedure. On the other hand, if the dwell time is too long, the scan will be very time consuming with little additional accuracy. In order to produce acceptable results, the dwell time was selected as 32 µseconds for searching and 64 µseconds for measuring. These dwell time increments were selected on the basis of being the minimum time required to conduct a successful SEM-AFA scan. Typically, the measuring dwell time is larger than the search dwell time to ensure that the particles are detected and measured accurately.

Beyond the SEM-AFA imaging settings, the image threshold values were selected based on a manual examination of endorsed area through defining the particle maximum and minimum detection and measurement limits, represented in the Yellow and Green colors respectively, as seen in the Figure 10.

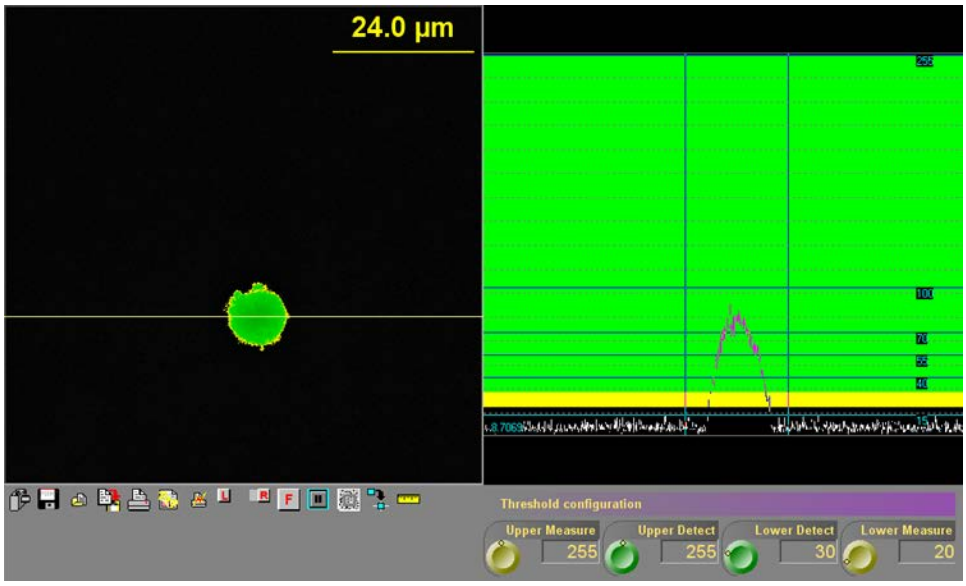

Figure 10: The threshold values applied on an individual fly ash particle. Green color represents measurement range while Yellow color represents detection range.

Both the Yellow and the Green color, seen in Figure 10, represent the image signal detection range by the BSD. The yellow color acts as a background phase, indicating minimum and maximum detection limits for images; these values are the thresholds used during the search process for fly ash particles. The green color represents the “true” threshold values; these values are the thresholds used during the measuring process. In this measuring process, each pixel is being measured and checked to determine if the pixel meets the threshold criterion; if it does it is considered to be a fly ash particle. The suitable thresholding values were found to be (255/30) for the measurement process and (255/20) for the search process as seen in Table 5. It should be mentioned that in back scattered images, zero corresponds for black and dark pixels, and 255 corresponds for white and bright pixels, and the range between both numbers corresponds to the different grey values. Therefore, it was expected in the SEM-AFA scan configuration that the search threshold region will have a bigger range than the measure threshold region.

Table 5- A summary of the image threshold values used during a typical AFA scan for fly ash particles

Thresholds Upper Measure (Green)	255
Thresholds Upper Search (Yellow)	255
Thresholds Upper Measure (Green)	30
Thresholds Upper Search (Yellow)	20

The completion of defining the different settings required during SEM-AFA scan for fly ash particles provides a reliable analytical tool capable of ascertaining a large volume of information for individual particles. For these individual particles the size and chemical composition will be investigated simultaneously.

SEM-AFA Consistency

A set of analyses were completed in order to quantify the consistency of the AFA analysis. At the beginning of the analysis the surface of the sample is manually checked for any signs of contamination using the SEM. Once a constant beam current is achieved, which is typically within 30 minutes of the SEM beam initiation, the SEM is set to capture images and collect EDS counts with a consistent performance. The constant beam performance is checked through measuring total beam electrical current charge flowing in vacuum for the scanning energy, which is 20 KV, using a faraday cup and pico-amp meter connected to it. The expected reading should be within the range of 1.4nA, as mentioned in Table 3. Three identical SEM-AFA scans were conducted on a stub of fly ash. The area scanned was divided into nine equal square fields by the SEM, as seen in Figure 11.

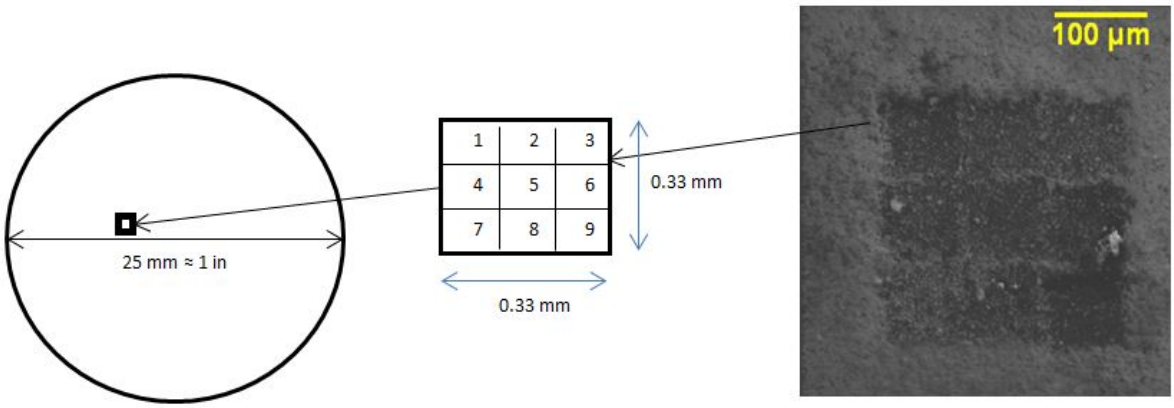

Figure 11: An illustration of the scanned area on the SEM coupled with SE image of the same area

Out of these repeated scans there were three particles that were not found in all of the scans. These particles were near the edges of the scans and were manually removed from the data sets for comparison. 90 matching particles were detected in all three scans.

The following graphs show the comparison between three scans in diameter, area and perimeter of the 90 matching particles. Each of these morphological outputs was measured by the SEM during the measuring dwell time of 64 micro seconds per pixel.

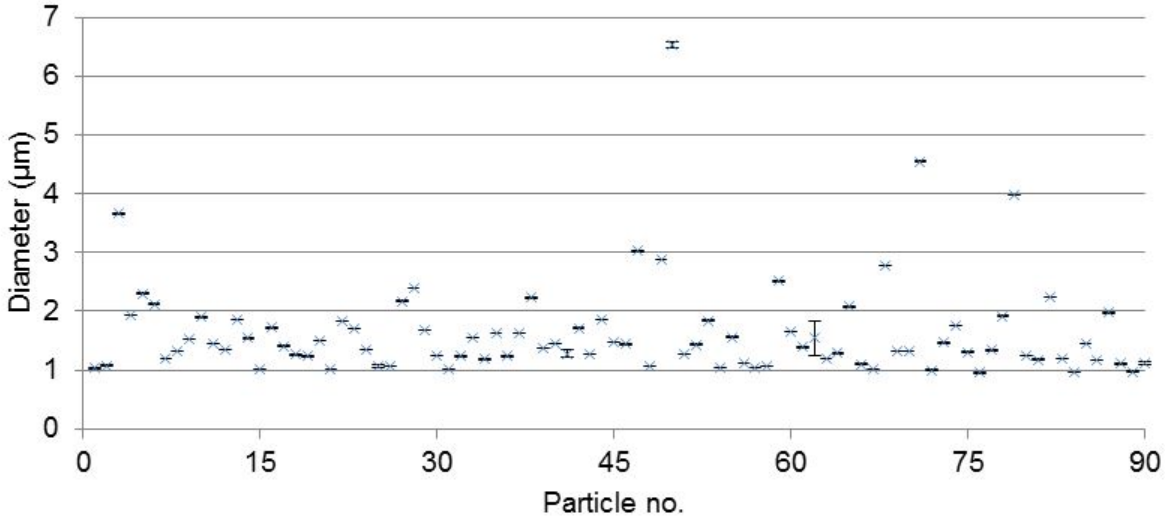

Figure 12: Diameter comparison for three scans of the same fly ash sample. Error bars with one standard deviation are shown.

In Figures 12, 13 and 14 there is a very small variance for all of the particles investigated under the three morphological parameters.

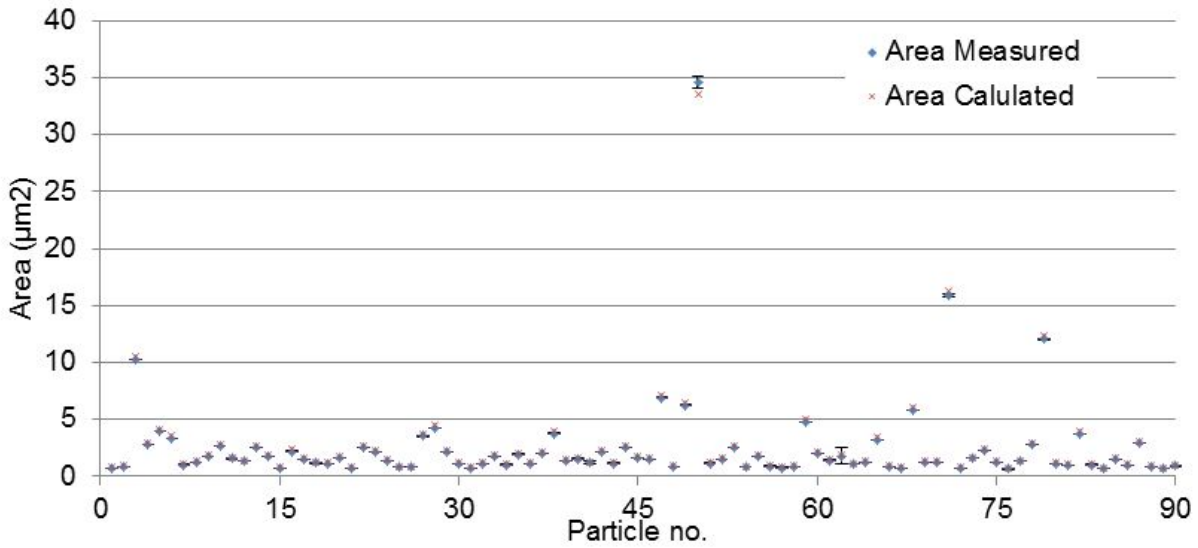

Figure 13: Area comparison for three scans of the same fly ash sample. Error bars with one standard deviation are shown.

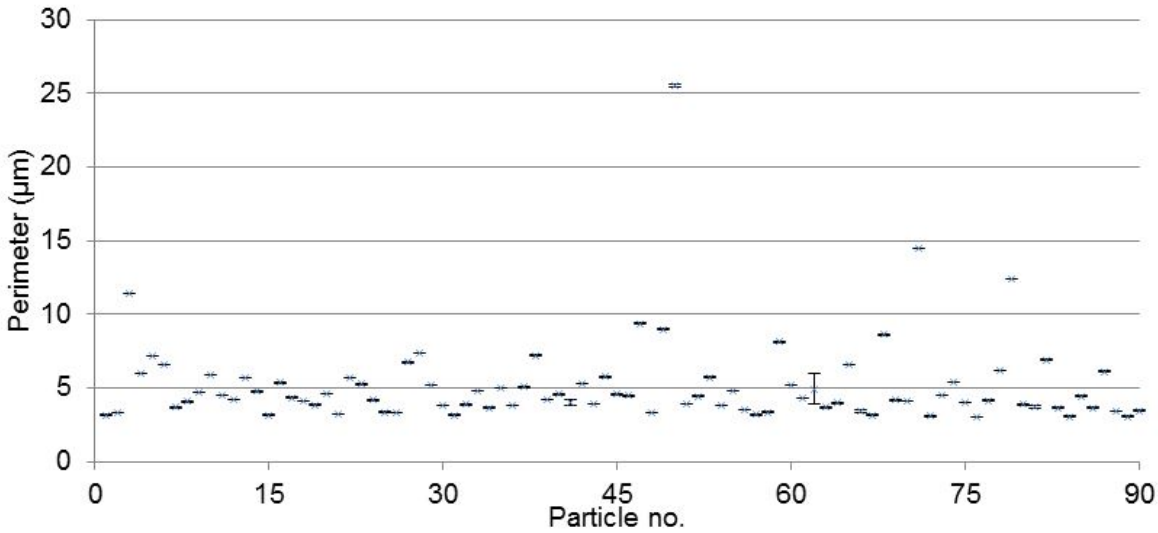

Figure 14: Perimeter comparison for three scans of the same fly ash sample. Error bars with one standard deviation are shown.

By comparing the particle size properties for all three scans, it was found that diameters for all particles investigated had an average coefficient of variation equal to 0.71%, while it was 1.47% for the area and 1.05% for the perimeter. In addition, it was found these settings were capable in giving identical images for the same fly ash particle collected from each of the three scans, as seen in the following three images, Figure 15.

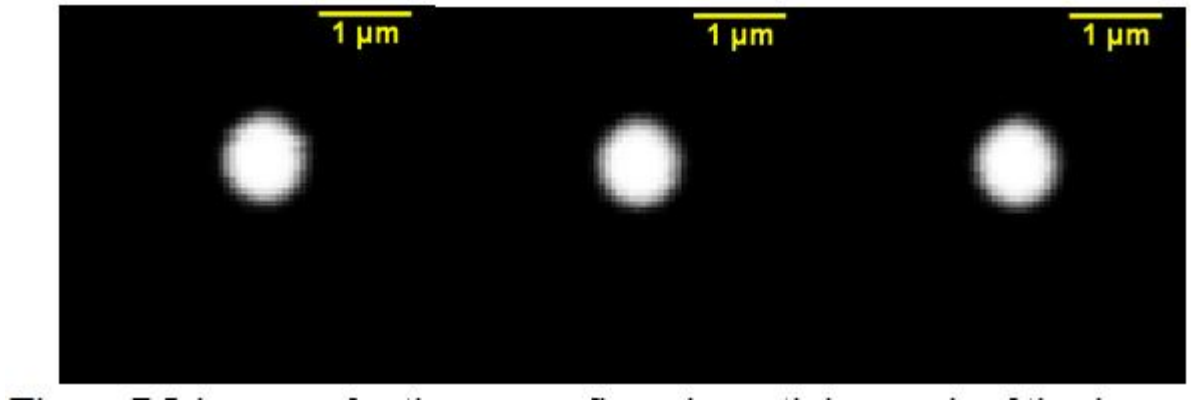

Figure 15: Three BS images for the same fly ash particle, each of the images have been collected from one of the three scans conducted.

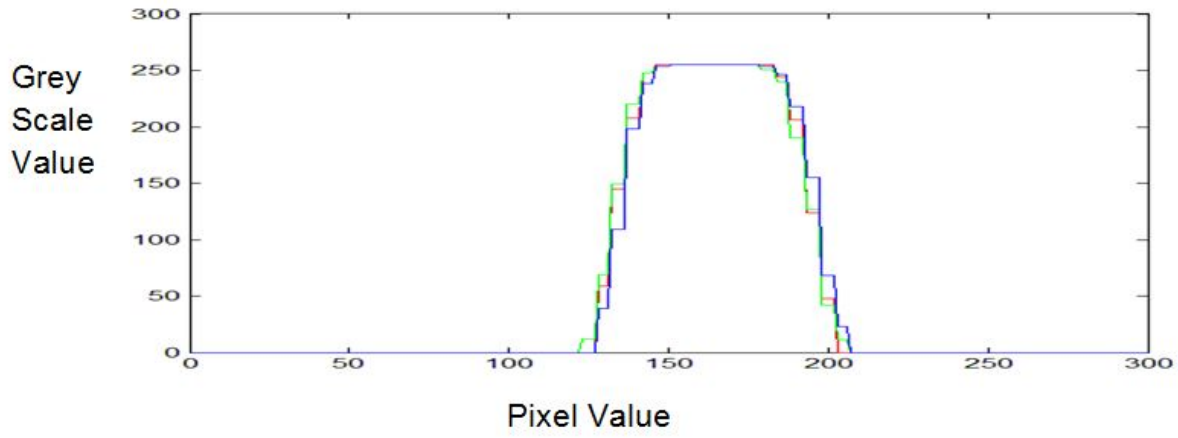

Figure 16: A line scan comparison between the three BS images for the same fly ash particle.

A virtual line scan was performed for all three images or specifically particles, seen in figure 16, which are for the same fly ash particle; each of those images was collected from one of the three different scans conducted. In this line scan, a line has been drawn passing through the center of particles while maintaining the same orientation for all three of them in order to obtain a grey scale histogram for each of the particles. The outcome, as seen in Figure 16, certified the success of the SEM-AFA scan settings in giving identical images with an equal resolution for each scan conducted.

The following graphs, Figures 17and 18, offer a comparison between the results from the EDS detector throughout the three AFA-SEM scans on the class C fly ash

stub. The live time and total counts where measured three times, and results were graphically plotted. Live time is the acquisition time required for collecting the incoming counts. It was found that the live time per particle for all three scans was identical with a uniform 5 second detection period per particle, as seen in Figure 17.

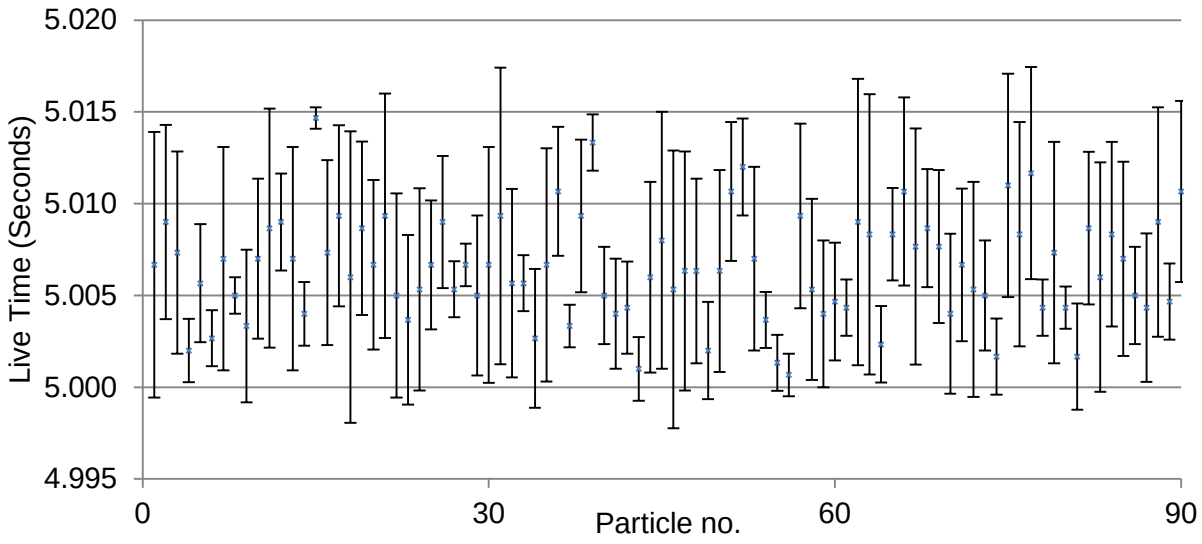

Figure 17: Live Time per particle comparison from three different scans.

The counts per second, seen in Figure 18, are a measurement of the amount of information being collected at any given point in the scan over time. It was found that the highest number of counts for a fly ash particle detected during the three scans was 32000, the lowest was 11000 counts per particle, and the average was 16500 counts per particle.

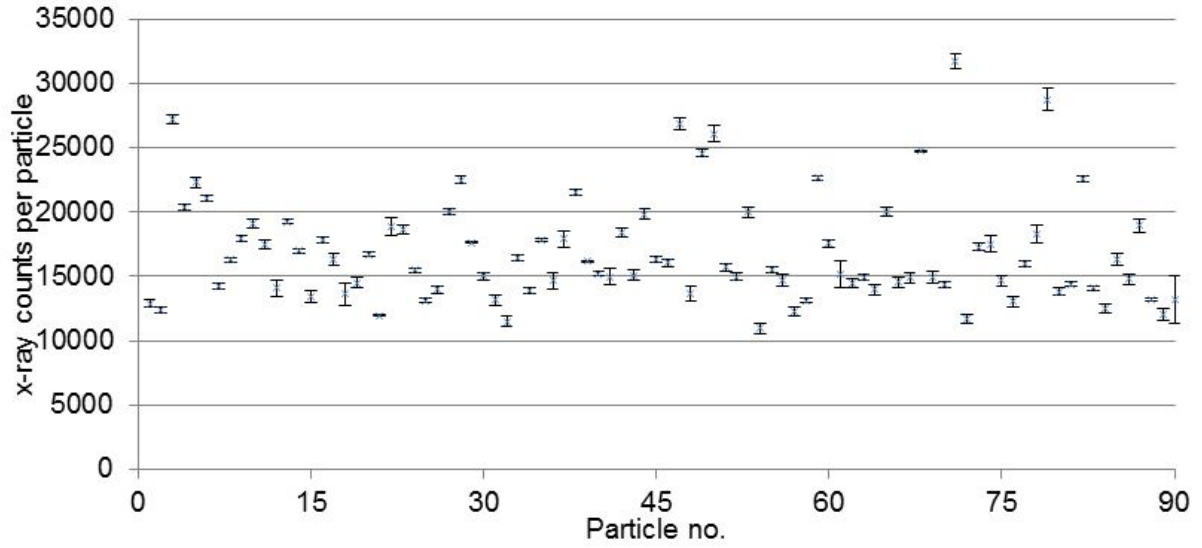

Figure 18: Total no. of counts per particle comparison

It should be noted that as the live time per particle increased from three seconds to five second as a detection period, the counts became higher and tighter in variation as seen in figure 18. This conclusion was based on a study conducted on 2.9 µm fly ash particle. This increase in collection time reflects an improvement in measurement statistics, enabling a sufficient gathering of the counts for each element per particle.

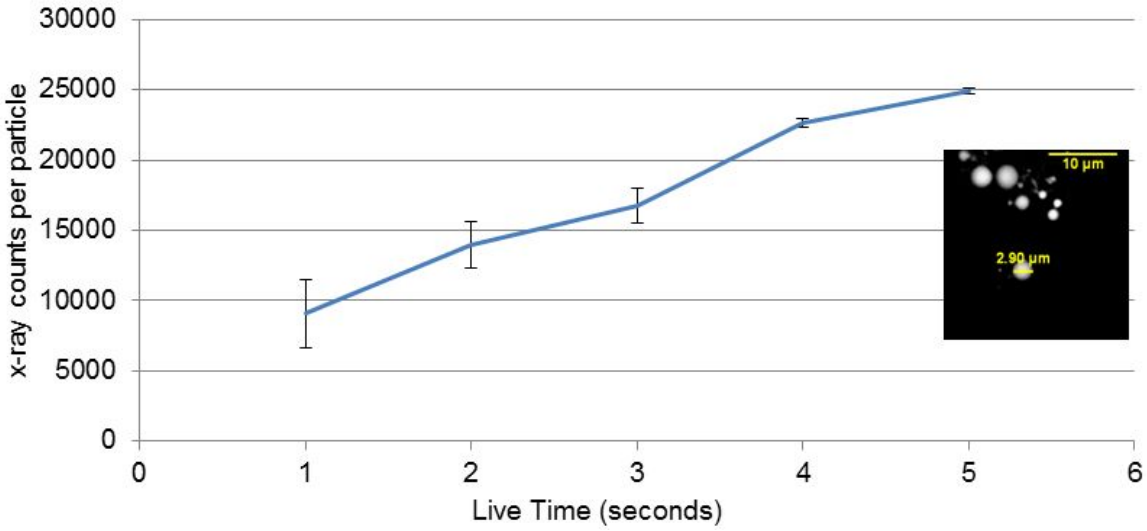

Figure 19: The relation between live time and x-ray counts per particle.

In Table 6 the highest element per particle was reported for each of the 90 particles detected. The highest element per particle was reported on bases of the counts per particles collected. It seems that the counts per element detected are the same for all particles addressed except for particle 61 and particle 90, which both had a coefficient of variation within the range of 10, with values of 11.7 and 9.7 consecutively.

Table 6 -The highest element and the corresponding no. of counts per particle for all three scans

Particle no.	Major Element	Scan no.1 (C/P)	Scan no.2 (C/P)	Scan no.3 (C/P)	Average (C/P)	S.D (C/P)	C.O.V
1	Ca	3313	3296	3336	3315	10	0.3
2	Ca	4019	4310	4123	4151	146	3.5
3	Ca	11430	11010	11420	11287	213	1.9
4	Ca	4716	4460	4656	4611	129	2.8
5	Si	9567	9439	9781	9596	83	0.9
6	Al	6053	5747	5935	5912	153	2.6
7	Si	3399	3494	3368	3420	50	1.5
8	Si	8089	8340	8283	8237	126	1.5
9	Si	4841	4984	4941	4922	72	1.5
10	Si	9644	9820	9611	9692	91	0.9

Particle no.	Major Element	Scan no.1 (C/P)	Scan no.2 (C/P)	Scan no.3 (C/P)	Average (C/P)	S.D (C/P)	C.O.V
11	Al	4407	4303	4454	4388	55	1.3
12	Ca	5144	4931	4679	4918	127	2.6
13	Si	5274	5203	5061	5179	49	1.0
14	Ca	5714	5693	5857	5755	31	0.5
15	Ca	3628	3580	3724	3644	33	0.9
16	Ca	5932	5586	5582	5700	176	3.1
17	Ca	5490	5052	5296	5279	219	4.1
18	Ca	4277	4711	4304	4431	220	5.0
19	Ca	5051	5127	5445	5208	78	1.5
20	Al	3605	3395	3599	3533	107	3.0
21	Ca	3400	3442	3399	3414	21	0.6
22	Ca	6662	6595	6646	6634	34	0.5
23	Al	4368	4281	4366	4338	44	1.0
24	Si	3370	3494	3367	3410	63	1.9
25	Si	2789	2586	2744	2706	102	3.8
26	Si	3228	3134	3282	3215	51	1.6
27	Si	4770	4671	4630	4690	52	1.1
28	Ca	8664	8549	8508	8574	61	0.7
29	Ca	6254	5941	6596	6264	184	2.9
30	Ca	4083	4096	4324	4168	46	1.1
31	Si	5195	5355	4951	5167	101	2.0
32	Ca	3432	3239	3181	3284	101	3.1
33	Ca	5157	5227	5147	5177	36	0.7
34	Ca	4234	4264	4631	4376	75	1.7
35	Si	4557	4460	4323	4447	60	1.4
36	Si	4730	4676	4671	4692	28	0.6
37	Si	4256	4052	4291	4200	105	2.5
38	Ca	6346	6347	6469	6387	24	0.4
39	Si	3859	3744	3617	3740	68	1.8
40	Ca	4254	4191	4567	4337	73	1.7
41	Si	3238	3572	3399	3403	167	4.9
42	Si	4029	4238	4047	4105	106	2.6
43	Al	3281	3228	3105	3205	39	1.2
44	Si	6666	6929	6627	6741	136	2.0
45	Si	4691	4666	4470	4609	42	0.9
46	Ca	3492	3815	3615	3641	162	4.4
47	Ca	6671	6232	6733	6545	226	3.5
48	Si	5437	5285	5582	5435	87	1.6
49	Si	10500	10370	10290	10387	71	0.7
50	Ca	9009	8836	8605	8817	106	1.2
51	Si	3339	3264	3190	3264	43	1.3
52	Ca	4478	4747	4761	4662	138	2.9
53	Al	5529	5439	5309	5426	56	1.0

Particle no.	Major Element	Scan no.1 (C/P)	Scan no.2 (C/P)	Scan no.3 (C/P)	Average (C/P)	S.D (C/P)	C.O.V
54	Ca	2154	2072	1901	2042	58	2.8
55	Ca	5168	5495	5353	5339	164	3.1
56	Si	3246	3300	2998	3181	59	1.9
57	Ca	4201	4379	4435	4338	93	2.1
58	Ca	3672	3682	3539	3631	27	0.7
59	Ca	8835	8734	8797	8789	51	0.6
60	Ca	6262	6269	6419	6317	30	0.5
61	Ca	3662	4657	4487	4269	501	11.7
62	Ca	4625	4399	3453	4159	233	5.6
63	Al	3367	3359	3290	3339	15	0.4
64	Si	6334	6189	6217	6247	73	1.2
65	Ca	6704	7025	6764	6831	162	2.4
66	Si	3351	3035	3182	3189	158	5.0
67	Si	2833	3024	3124	2994	103	3.4
68	Si	11900	11560	11750	11737	170	1.4
69	Ca	5027	4922	4852	4934	58	1.2
70	Ca	4739	4303	4382	4475	220	4.9
71	Al	11260	10940	10690	10963	178	1.6
72	Ca	3530	3423	3393	3449	56	1.6
73	Al	3965	4112	3924	4000	77	1.9
74	Ca	5407	5754	5656	5606	174	3.1
75	Ca	4457	4333	4160	4317	77	1.8
76	Si	2712	2815	2686	2738	54	2.0
77	Si	3669	3928	3545	3714	138	3.7
78	Ca	4931	5133	5231	5098	108	2.1
79	Ca	10110	10480	9624	10071	226	2.2
80	Ca	3942	4226	4673	4280	182	4.2
81	Al	3094	3143	3245	3161	35	1.1
82	Ca	7159	7095	7345	7200	53	0.7
83	Ca	4249	4081	4152	4161	84	2.0
84	Ca	3979	4057	3875	3970	48	1.2
85	Si	4110	4374	4205	4230	132	3.1
86	Al	3326	3286	3385	3332	25	0.8
87	Ca	7238	7315	7289	7281	39	0.5
88	Si	4773	4705	4602	4693	43	0.9
89	Ca	3810	3942	3952	3901	68	1.7
90	Ca	5088	4252	4090	4477	433	9.7

By achieving such consistency, as observed in Figure 12, 13, 14, 16, 17 and 18 in addition to Table 5, it seems that the adopted settings performance has been approved, ensuring the ability of this methodology to meet the requirements and

achieve highly repeatable data. Next these techniques were used on five commercial types of fly ash.

Morphological Comparison

In AFA-SEM result comparison, 2000 particles from each type of fly ash were scanned under the same settings and identical conditions. Five different commercial types of fly ash are considered within this study, three of these fly ashes are classified as C, one is F, and last is C/F according to the ASTM C618 metal oxide quantification. In this report, a comparison made between the different fly ash is correlated to different particle diameter. Figure 20 represent a graphical plot between different particle size ranges up to 75 µm and their frequency for all five commercial types of fly ash. By comparing the different plots, it seems that 80% of the C3 are smaller than 2 microns in diameter. While F, C/F, and C1 fly ash particles that are smaller than 3 microns in diameter represent over 80%. It seems also that C2 had particles smaller than 5 micron representing over 80%. In summary, Table 7 represents the average diameter for particles smaller than 75 µm for the five commercial fly ashes studied.

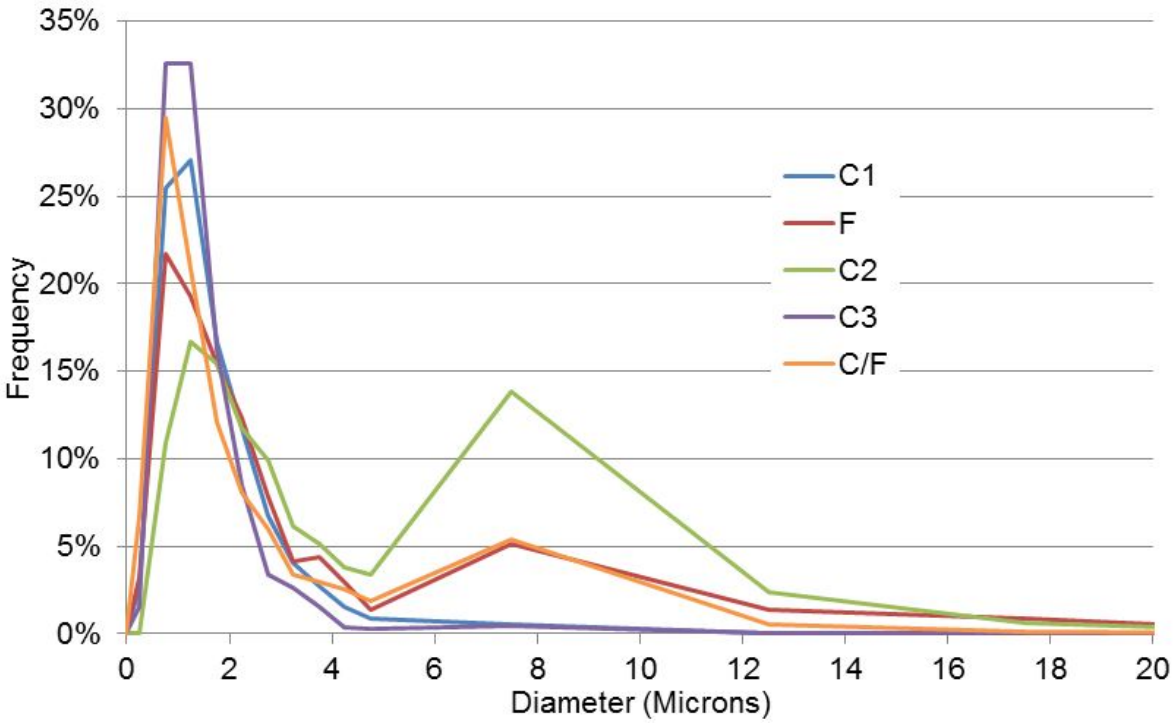

Figure 20: Diameter vs Frequency for particles smaller than 75 microns

Table 7 -The average diameter for the 5 commercial types of fly ash

	Average Diam. (μm)
C1	1.64
F	2.38
C2	3.16
C3	1.40
C/F	1.90

In addition the size of each particle can be correlated to the chemistry. The authors feel that this information may provide insight into why different sources of fly ash have different performance in concrete. The graph in figure 21 represents the different particle size ranges versus their frequency for the three most dominant fly ash elements for C3 fly ash powder, while Table 8 contains the results for all five commercial types of fly ash. In this table, for each type of fly ash the maximum frequency diameter for that specific type of ash is recorded followed by the dominant diameter for calcium rich particles, then silicon rich particles and lastly aluminum particles for this commercial type of ash. This was conducted for all five commercial types of ashes. Finally, it should be mentioned that the study of maximum frequency versus diameter was conducted with 0.25 μm increments.

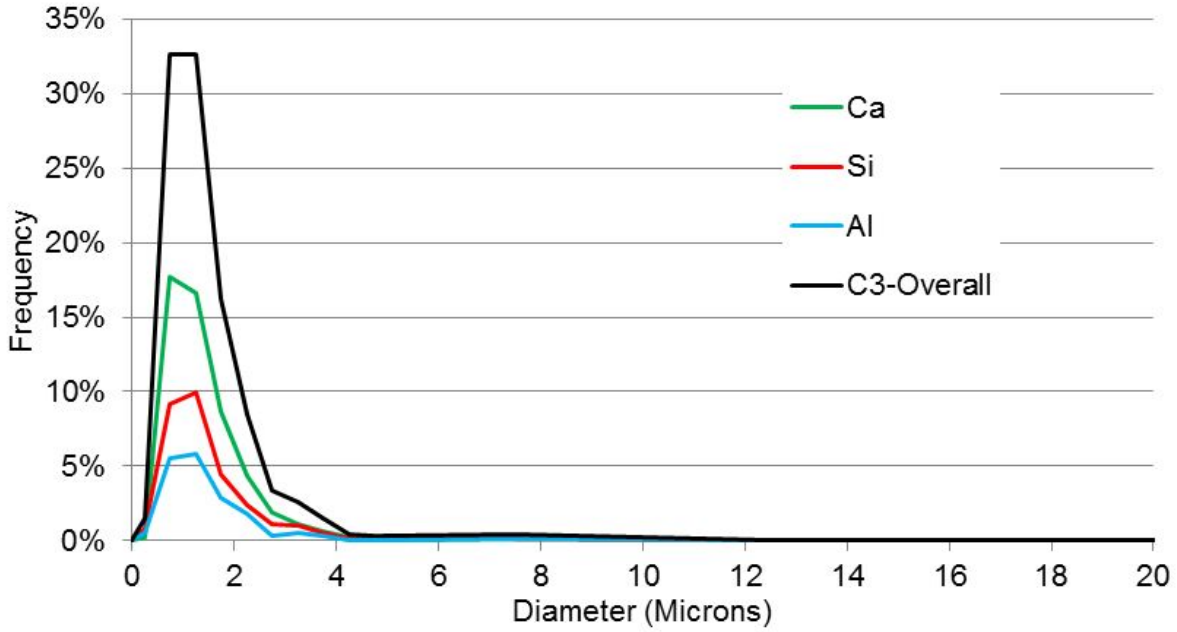

Figure 21: Diameter vs Frequency for C3 fly ash for the three most dominant elements

Table 8 - Maximum-in-Frequency Diameter for the 5 commercial types of fly ash

	Overall (All Particles)		Ca Rich Particles		Si Rich Particles		Al Rich Particles	
	D. (µm)	M. F.	D. (µm)	M. F.	D. (µm)	M. F.	D. (µm)	M. F.
C1	1.25	27.1%	1.25	11.5%	1.25	10.9%	1.25	4.7%
F	0.75	21.7%	0.75	4.7%	0.75	13.2%	0.75	3.7%
C2	1.25	16.7%	7.5	8.6%	1.25	4.6%	1.25	5.0%
C3	1	32.6%	0.75	17.7%	1.25	10.0%	1.25	5.9%
C/F	0.75	29.5%	0.75	6.8%	0.75	14.1%	0.75	8.5%

Table 8 summarizes Figure 21 for all five commercial types of fly ashes addressed in this document. Each of the major three elements is being investigated separately for each of the five fly ashes in order to evaluate the diameter frequency from these major chemical elements. It seems from Table 6 that all class C particles, including C1 - C2 - C3, had calcium rich particles as the most dominant rich particles for these three ashes, with maximum frequency of 11.5%, 8.6% and 17.7% at 1.25, 7.5 and 0.75 µm consecutively. On the other hand, in class F and C/F silicon rich particles were the most dominant with 13.2% and 14.1% at 0.75 µm. It should be mentioned that C1, F and C/F had nearly perfect matching peak pattern regarding their calcium, silicon and aluminum dominant particles, with the peak occurring where it occurred at 1.25, 0.75, and 0.75 µm consecutively as seen in Table 8.

Also from Table 8, it seems that particles smaller than 1 µm in diameter were frequently calcium rich particles for all five fly ashes except for C2. The distribution of both silicon and aluminum rich particles had an identical performance pattern throughout the five ashes. This distribution pattern can be divided into two distinct groups where all Class C had maximum frequency at diameter nominal size of 1.25 µm for both silicon and aluminum rich particles. The other group contained both F and C/F ashes only, where the maximum frequency took place at a diameter of 0.75 µm for both silicon and aluminum rich particles.

Additionally, it has been observed that roundness of fly ash particles is not limited to a certain size of ash particles, as seen in Table 9, where the average aspect ratio (AAR) for almost all five commercial types of fly ash was in the range of 1.1 ± 0.03 except for C2 particles that are smaller than 1 µm, whichhad an average aspect ratio of 1.2. Finally, fly ash particles ranging from 1 to 40.5 µm in geometric diameters tended to be more spherical than particles less than 1 µm.

Table 9 -Diameter range vs average aspect ratio (AAR) for the 5 commercial types of fly ash

Diam. Range	0.1 - 1 µm	1 - 5 µm	5 - 10 µm	10 - 40.5 µm
	AAR	AAR	AAR	AAR
C1	1.13	1.08	1.09	N/A
F	1.11	1.09	1.10	1.12
C2	1.20	1.12	1.09	1.09
C3	1.13	1.09	1.08	N/A
C/F	1.12	1.11	1.13	1.12

Chemical Comparison

Figures 22, 23 and 24 describe what we define as silica, aluminum, and calcium based particles, shown consecutively. In Figure 25 the normalized spectrum of three fly ash particles with one of the three different primary elements can be observed. The particles chosen are from the first image on the left in Figures 22, 23 and 24**.** The spectrum consisted mainly of C, O, Mg, Al, Si and Ca[15-18], with smaller amounts of other minor elements such as Na, P, S, K and Fe[10,17-19]. Figure 25 illustrates the percentage of raw counts normalized for each particle.

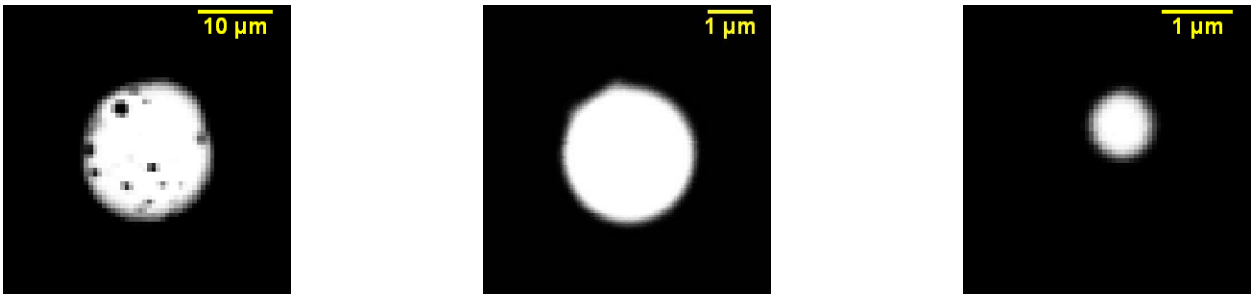

Figure 22: BS image for the Si rich fly ash particles.

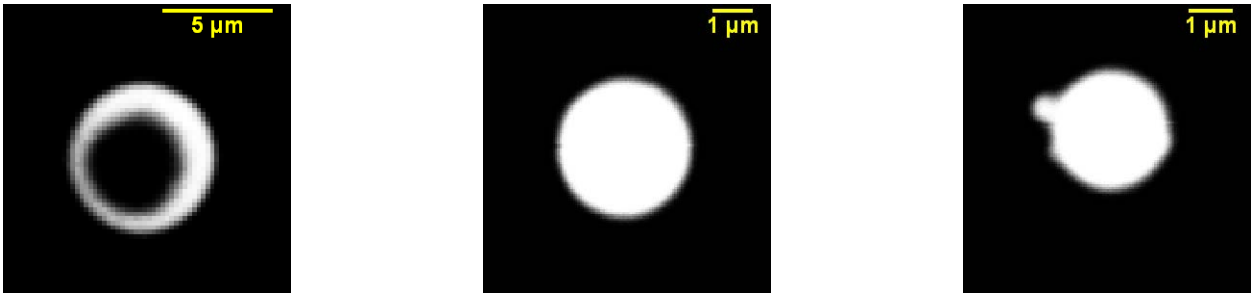

Figure 23: BS image for the Al rich fly ash particles

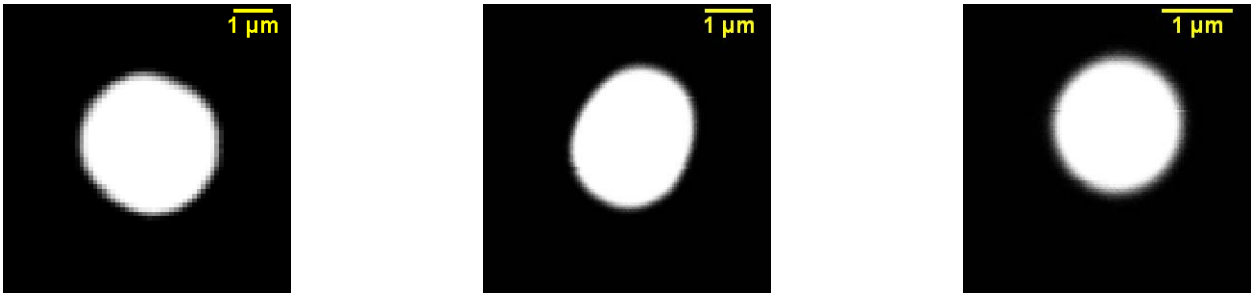

Figure 24: BS image for the Ca rich fly ash particles.

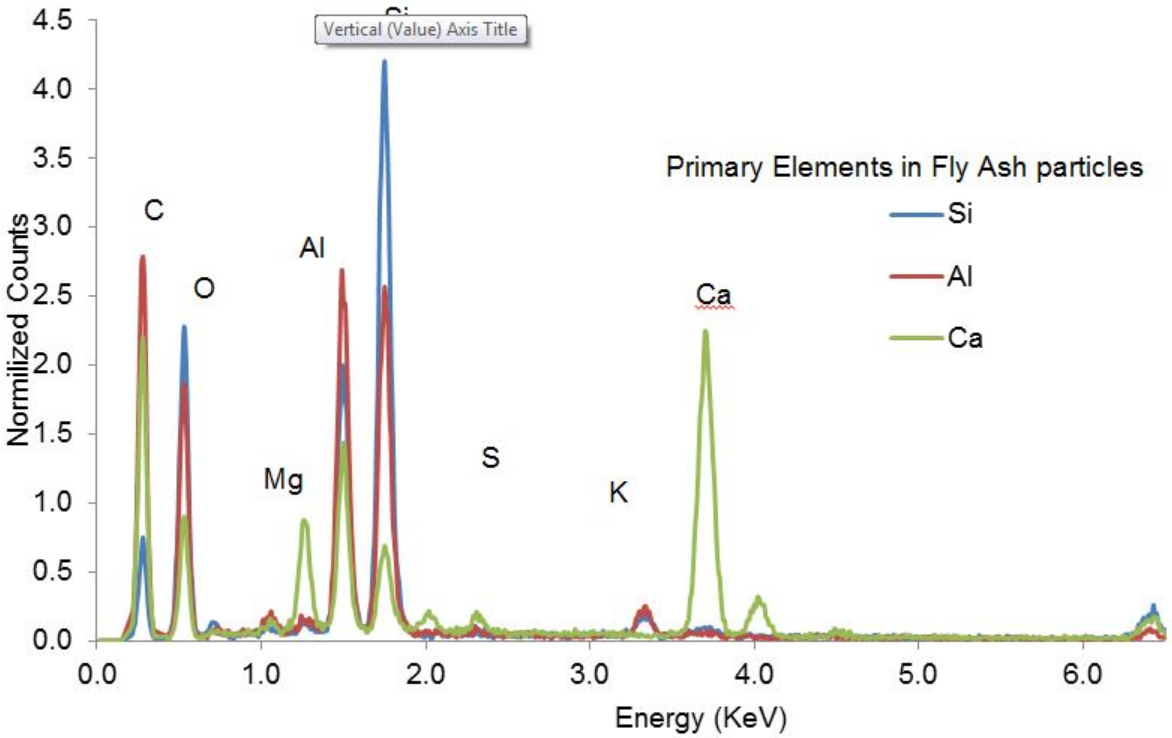

Figure 25: A comparison between a typical Si rich particle, Al rich particle and Ca rich particle

An assessment comparing the major highest elements detected in 2000 fly ash particles was conducted and plotted in Figure 26. The percentage of the highest element detected in 2000 particles for each type of Fly ash is based on the number of counts collected for an element. Estimating the mass percentages was based on defining the highest element in counts collected per particle, then summing up all the particles that had the same element as its highest and labeling such a group based on that element. It could be said that all five ashes had a minimum of 40% as calcium dominant element particles, while C/F had only 30%, and F was even lower with a value

of 18%. However, for silicon dominant element particles, all class C particles had a maximum contribution of 40% conceding with C/F, while class F seemed to have the highest concentration of silicon dominant particles with contribution exceeding 65%. Aluminum represented the third highest element in fly ash within this study with a very variable content. The highest type of fly ash with aluminum dominant particles was C/F with contribution reaching almost 30%. The last two elements, iron and sodium, did not represent a high concentration as dominant elements; however they had a more integral role as secondary elements.

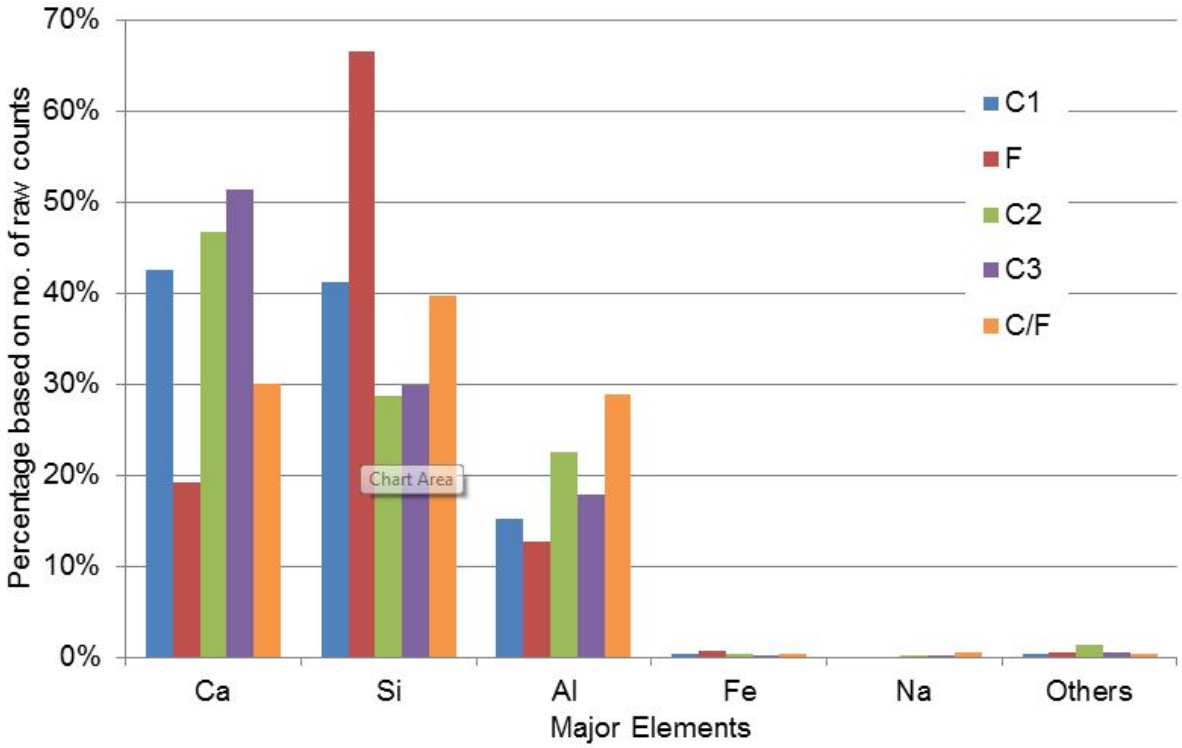

Figure 26: Major elements corresponding to the highest no. of counts detected in the AFA Scans

The following graph, in Figure 27, shows the bulk XRF values for for the element oxides of the same major elements detected in the 2000 particles per fly ash. It should be noted that class C fly ashes maintained a superior performance regarding calcium oxide concentration over F and C/F classes, similar to what has been observed in the SEM-AFA results. Also, class F had a higher concentration of silicon dioxide in it bulk XRF result compared to class C and C/F, which matches with the SEM-AFA results. Consequently, F had strong peaks of silicon which is typical in low lime ash, while all C's had strong calcium peaks which is expected for high lime ash. C/F had almost equal peaks of calcium, aluminum and silicon.

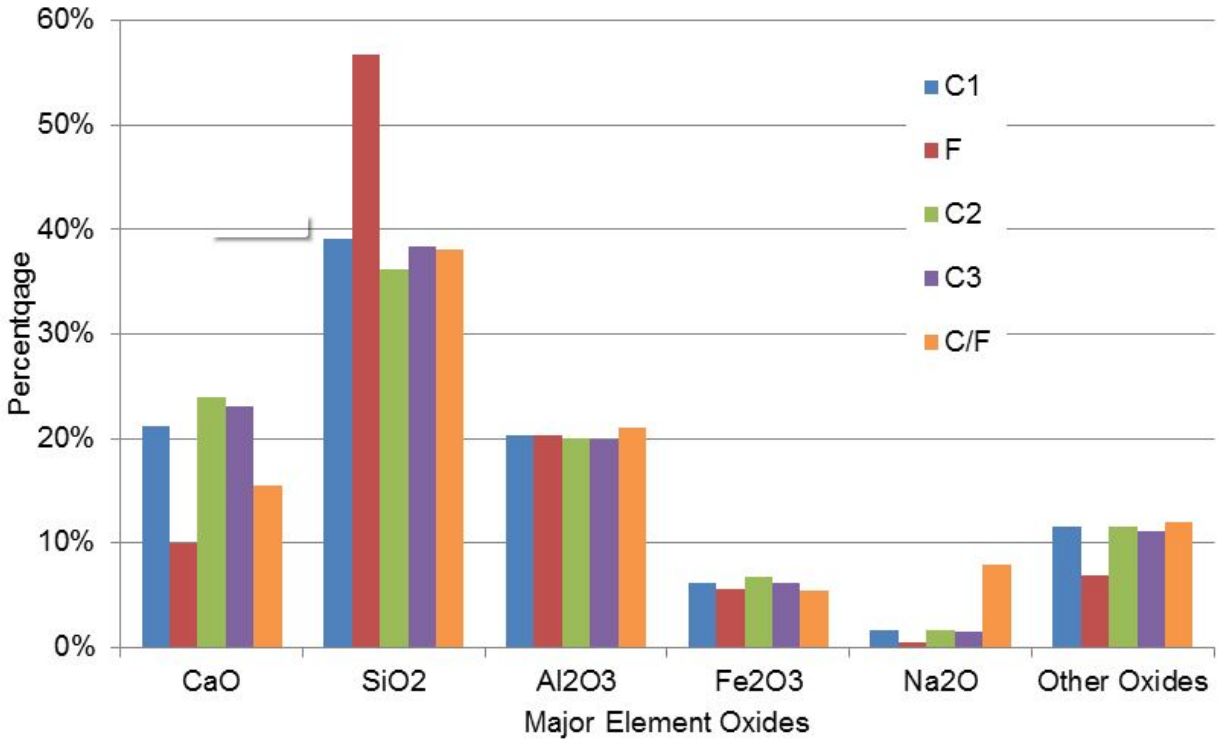

Figure 27: Bulk XRF for Major Elements

From Figures 26 and 27, it seems the elemental concentrations, as determined by EDS, were consistent with XRF oxide values up to limit. It should be remembered that XRF offers an average overall chemical composition for fly ashes without taking into consideration the diverse phase composition of the individual particles, which SEM investigates through this SEM-AFA technique.

Similar to Figures 26 and 27, Figures 28 and 29 were plotted for the minor elements and minor element oxides consecutively. By comparing the results from the SEM-AFA in Figure 28, it seems that there are only two minor dominant elements that are consistent throughout all of the seven commercial types of fly ash; these elements are iron and titanium. Although, of the variable performance of the different types of fly ash regarding their minor elemental concentration, it seems class F has a higher concentration of iron as dominant element than any other type of fly ash. Similarly, class C/F has a higher sodium concentration than any other type of fly ash. By correlating this information to bulk XRF values for the same minor elements in Figure 29, difference and similarities can be detected. For example ferric oxide does not preserve a higher concentration in class F compared to other classes as observed in the SEM-AFA output. On the other hand, sodium oxide shows superiority in concentration for class C/F, matching with SEM-AFA results.

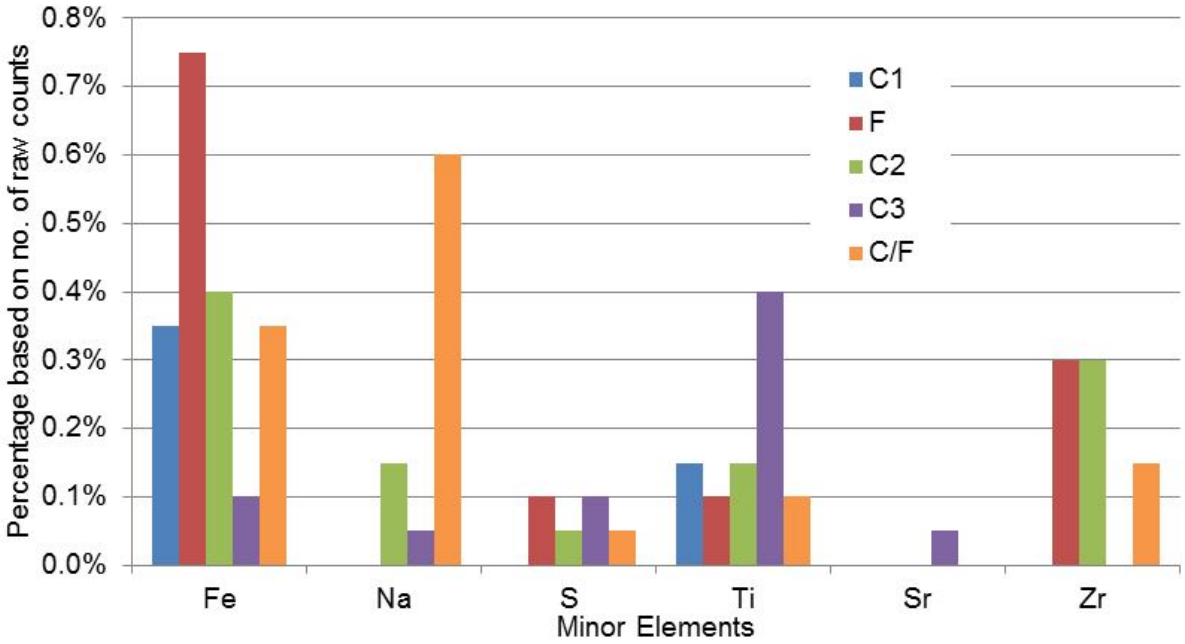

Figure 28: Minor elements corresponding to the highest no. of counts detected in the AFA Scan

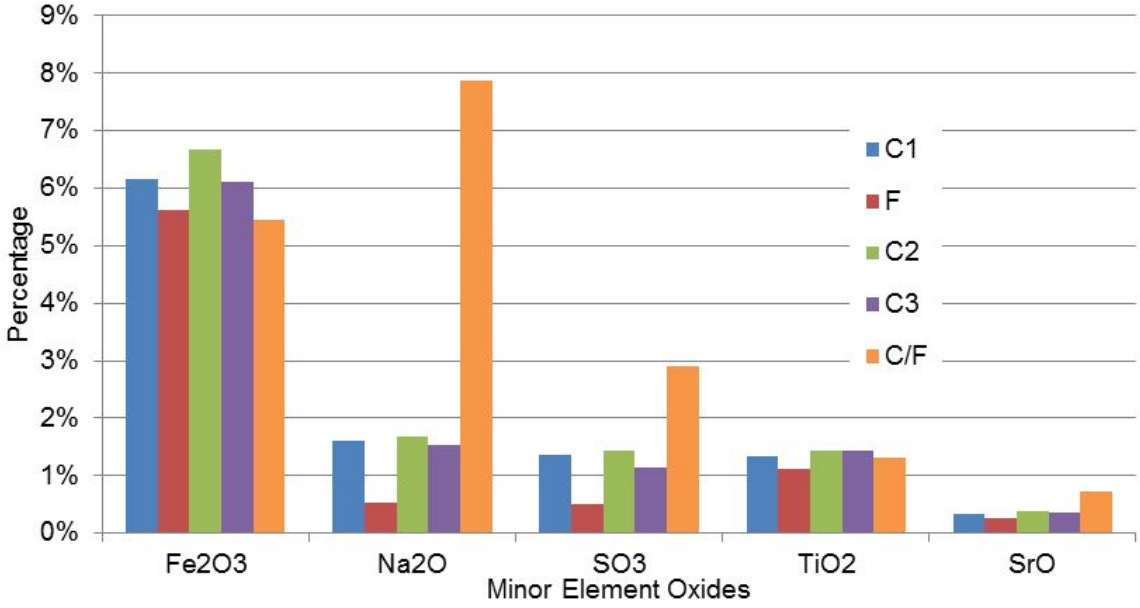

Figure 29: Bulk XRF for Minor Elements

Future work

Additional work is still needed to improve this technique. Necessary improvements are described below.

Armstrong Correction

EDS is a surface reference method but certainly not a surface analysis technique; therefore, all the qualitative analyses obtained using the EDS detector are based on the assumption that the electron beam is exciting fly ash particles with different sizes and material composition at a homogeneous volumetric rate. However, this is not correct, as the variability of fly ash particles creates lots of difficulties to fly ash particles smaller than 10 microns. Therefore, a correction matrix must be applied to those particles; this intensity correction matrix is known as the Armstrong Correction. The Armstrong Correction works on resolving these issues mathematically. This is conducted through resolving the error histograms caused by inaccurate “conventional” particle analysis procedures by geometric-correction approach which causes the errors to shrink greatly. The correction results are time consuming and have not been included in this report. More information and results will be offered in future work.

Clustering

Fly ash powder is a complex material. The ability to characterize and determine the chemical composition and morphology at such an intimate scale is a very powerful tool. Cluster fly ash particles on the possibility to identify characteristic group with similar composition. These clusters can be used to develop standard sets of fly ashes based on the major chemical constituents and the major morphological properties, therefore, characteristic reactivity fly ash groups will be formed. This approach could be the basis for a more accurate description of fly ash which could be later on attributed to the original chemical composition of the coal.

Using the SEM-AFA scans, a huge data base will be built for thousands of diverse and complex particles. This clustering process is an ongoing process until more precise defined clusters are achieved.

Combination with physical testing results

This project also includes the development of fly ash within the concrete performance-based classification system. This system depends on concrete mixtures’ performance when subjected to standardized physical testing procedures.

Summary

The ASEM technique has shown the ability to define the presence of fly ash elements within its structure in a repeatable fashion. This enabled enhancing the project outcomes. In conclusion, this research is an effort in a lengthy process to find out ways to further define fly ash particles beyond the typical ASTM C618 classification of C and F in order to utilize its usage in the concrete industry. Simply, this technique takes a great step towards achieving a better way of defining fly ash and understanding it as a material.

CHAPTER 3 - USE OF MICRO TOMOGRAPHY TO INVESTIGATE FLY ASH

This chapter presents a new analytical technique that uses a combination of electron probe microanalysis (EPMA) based microanalysis and micro X-ray computed tomography (μCT) to produce 3D maps of the microstructure and distribution of chemical constituents within complex particles. This methodology has been named **T**omography **A**ssisted **C**hemical **Co**rrelation or **TACCo** by the authors. This technique has the ability to identify different constituent phases and map their 3D location. While the work focuses on applying this technique to fly ash, TACCo applies to any material that can be investigated with both X-ray tomography and a scanning electron beam.

High flux electron beams are commonly used for elemental analysis of materials. An incident electron beam with sufficient energy will cause an atom to emit a characteristic photon through the photoelectric effect[9]. This information can be used to create detailed compositional maps of the surface of materials through the use of energy dispersive X-ray spectrometers[9-12]. To obtain reliable data with the technique a sample must be polished, conductive (or coated in conductive carbon), and analyzed in a high vacuum. While this technique, known as electron probe microanalysis (EPMA), is widely used, it has several challenges, as it can damage the sample at high probe currents (i.e. > 100 nA), only allows observations of the composition in the first few micrometers to be made, and must be viewed in a high vacuum environment[9-10.]

It is common in the medical sciences to use X-ray computed tomography to non-destructively image the internal structure of organisms. This technique uses a series of X-ray radiographs at small angles of rotation that are coupled to produce a 3D model[20-22]. While this technique does not provide direct compositional information about the irradiated materials, it does provide clues about compositional consistency. In the CT scan, solid materials with different mass absorption coefficients and densities will appear to have different gray values. However, this data does not provide a priori compositional information.

A new generation of tomography techniques is being used that allows the user to enter any domain and find the spatial resolution of unique chemical constituents by combining μCT with information from X-ray Fluorescence. These investigations have been found to require days to gain the data that is needed[23-24]. Furthermore, this technique is limited to 3D models at roughly 30 microns. The required investigation time for the TACCo analysis can be on the order of hours and produces 3D maps at the resolution size of the parent μCT and EPMA, with the current best resolution at 10s of

nm[25-26]. Furthermore, once the data has been fused between the μCT and EPMA, then one can continue to use only the μCT for 3D constituent information.

Currently, there is a need to better understand the composition and microstructure of complex particles. In this paper, large fly ash particles are used as examples of such materials. Fly ash is made up of crystalline and amorphous phases containing predominantly Al, Si, Ca and Fe[15-18]. The particles are generally spherical with diameters ranging from less than 1 μm to more than 1 mm[20]. Trace deposits of metals such as arsenic, cesium, lead, selenium, cadmium, and zirconium have been found within these materials[17-19] Fly ash is commonly used as a low cost construction binder for stabilization of soil, a partial replacement of portland cement in a concrete mixture, and the predominate binder in a geopolymer concrete[2-3].

The ability to characterize fly ash at an intimate scale provides new tools to understand, extend, and improve its usage. Specific needs to characterize the elemental makeup, the reactivity, and the location of these constituents within a particle will improve the use. This can have significant impacts on the economy, durability, strength, rheology, and sustainability of modern concretes. The majority of previous work has focused on the measurement of bulk properties of fly ash[4-7]. A few others have tried to characterize fly ash in more depth[8, 27.] This work provides unique details not previously possible.

These needs to characterize complex powders are not just common to the investigation of fly ash but are common to the study of catalysts, pharmaceuticals, ceramics, contaminated soils, asteroids, geologic materials, biomaterials, and others. While these materials have been investigated by either μCT or EPMA no previous publication has successfully fused this data. The presented methods could be useful for any material that can be analyzed by both μCT and EPMA.

Methods

A graphical summary of the methods used is shown in Fig. 30.

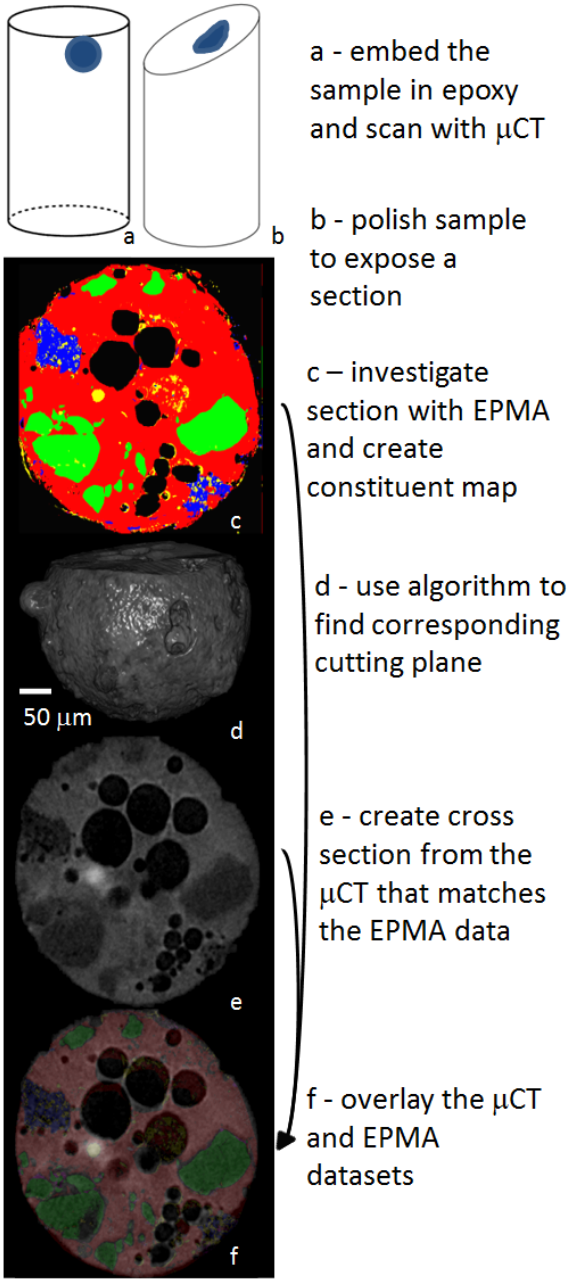

Figure 30: An overview of the processes used for fusing the EPMA and µCT data sets.

Sample Description and Preparation

This chapter investigates three fly ash particles from a single source. The fly ash is classified as ASTM C 618 class C. The results from the bulk XRF analysis is given in Table 10. Particles with diameters larger than 200 µm were used, as they were easy to handle and provided a sufficient area to provide a large compositional and µCT data set. The methods described can be used for any size particle as long as the analytical technique provides adequate resolution. Work on smaller particles will be included in future publications.

Table 10 – A powder XRF analysis for the fly ash investigated in this study.

SiO_2	36.21
Al_2O_3	19.94
Fe_2O_3	6.67
CaO	23.96
MgO	5.17
Na_2O	1.67
K_2O	0.52
TiO_2	1.44
MnO_2	0.03
P_2O_5	1.44
SrO	0.38
BaO	0.69
SO_3	1.44
L.O.I	0.15
Moisture	0.04
$SiO_2+Al_2O_3+Fe_2O_3$	63.12
ASTM C 618 classification	C

A plastic cylinder mold that is open on the top and bottom is filled with a low viscosity epoxy. The epoxy was chosen as it is easy to polish, has a low X-ray attenuation coefficient, and shows minimal outgassing in a vacuum. Before the epoxy hardened, a fly ash particle was placed on the surface of the freshly mixed epoxy and allowed to sink to the bottom. The specimen was then left for a day to harden. A drawing of the specimen is shown in Fig. 30a.

Micro Computed Tomography

After the particle is embedded in epoxy it was then investigated with a laboratory SkyScan 1172 µCT scanner. A parametric study is summarized in the supplementary information that was completed to find the setting that provides the highest quality images. Scans were made at 0.3^{o} of rotation step over 180^{o} and with a 5 frame/step averaging rate. In all scans, the voltage was modified so that a transmission rate of 27.5% was required at the center of the particle. The minimum transmission was used as opposed to voltage or power because each fly ash particle may be of different composition and size. Radiographs of 1000 pixel x 1000 pixel were used to create tomography models for the trials with a 5 µm voxel size. Scans were done with the filters of 0.5 mm aluminum, 0.5 mm aluminum with 0.5 mm copper, and none. Filters absorb lower energy X-rays and allow high energy X-rays to interact with the sample. This narrows the bandwidth of the X-ray source, reducing spurious signals to the X-ray detector and improving image quality. The benefit depends on the need to detect low absorption phases.

Tomography cross section images were evaluated for the presence of beam hardening artifacts and overall contrast of the images. For each evaluation, a quantitative comparison was made of the gray scale histogram. The 0.5 mm aluminum filter was found to provide the best reduction in artifacts and overall quality of image. Next, X-ray transmission rates between 20% and 40% were investigated for the sample to compare contrast and the quality of the radiographs. A transmission rate of 28% +/- 3% (one standard deviation) at the center of the particle was optimal for the materials, detector, and equipment.

With these settings, 4000 pixels x 4000 pixel radiographs were captured. This allowed tomography models to be reconstructed with a 1.05 µm voxel size. All reconstruction was completed with the SkyScan software NRecon. Both Drishti and Amira software packages were used for 3D visualizations[28,29]. A summary of the scan and reconstruction settings can be found in Table 11.

Table 11 – Scan settings from the µCT.

Parameter		Setting
Source Voltage		29 kev
Image Pixel Size		1.05 um
Filter		Al (0.5mm thickness)
Rotation Step		0.3 deg
Number of Frames Averaging		4
Dynamic range	Low	0
	High	0.73
Beam Hardening Correction		30%

It was important for this work to use the same instrument and reconstruction settings for all subsequent measurement techniques so that quantitative comparisons could be made. An example cross section can be found in Fig. 30e and a histogram of the gray scale values observed is shown in Fig. 31.

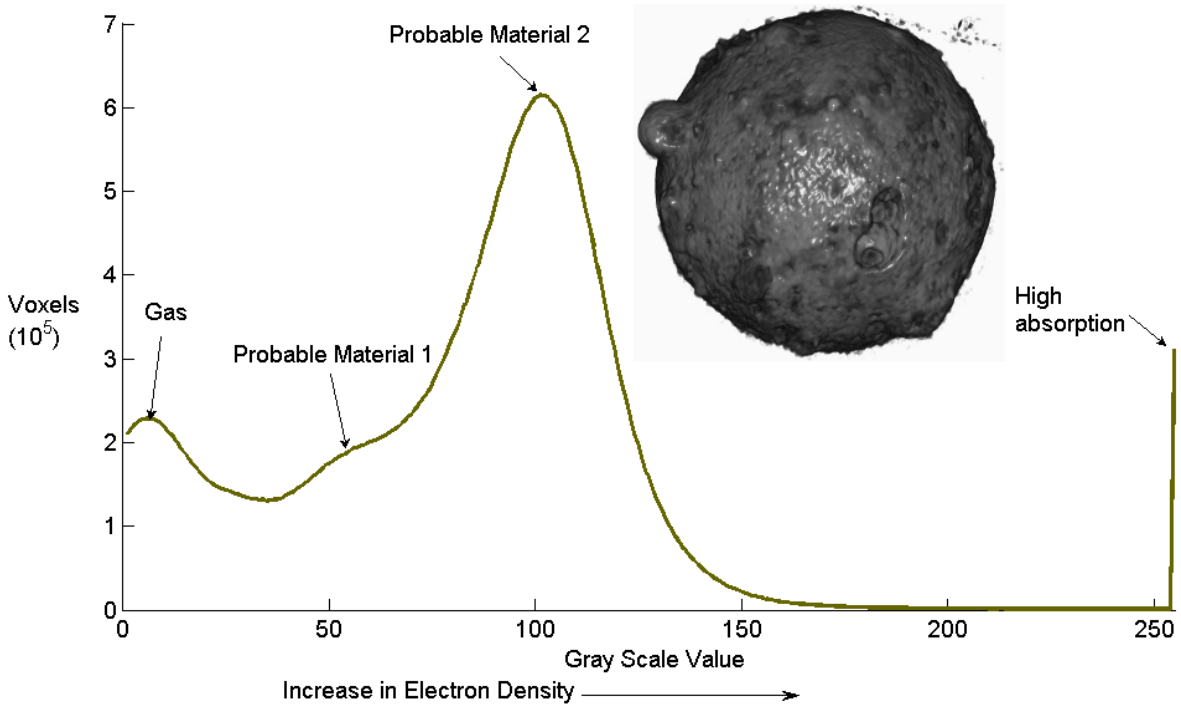

Figure 31: The number of voxels at different gray scale values from the 3D set for Particle 1C.

□CT data

Electron Probe Microanalysis

After investigating the sample with µCT, the epoxy cylinder is then polished with diamond pastes to expose a flat cross section as shown in Fig. 1b. The pastes used are water suspensions; however, the particles were not in contact with water for longer than 300 s during polishing. Elemental x-rays were produced in the first 4 µm of the sample surface, although higher energy bremsstrahlung x-rays were produced from a larger area.

Once polished, the exposed surface is then imaged with the backscatter electron detector and a Bruker Quad 4040 x-ray energy dispersive spectrometer (EDS). All x-ray data were taken using the JEOL 8500f electron microprobe at 20 keV accelerating voltage, with 50 nA of probe current. These settings produced a stored count rate of approximately 100,000 counts/s. The standards were collected at similar conditions, although the probe current was decreased on the pure elemental standards. The per-pixel dwell time was adjusted on each map to provide at least 20,000 counts in each spectrum. Dwell times were generally approximately 100 ms/pixel. The X-ray data are collected and stored in a hyperspectral binary data cube with a full X-ray spectrum at each point. First order approximations based on Monte Carlo calculations show that 95% of the elemental x-rays were produced in the first 4 µm of the sample surface, although higher energy bremsstrahlung x-rays were produced from a larger area. For all particles studied, the experimental conditions were held constant.

The initial output from this analysis is a backscatter image and a series of elemental images, derived based on raw elemental counts. Examples of the resulting images can be seen in Fig. 3 for particle 1C. While this information is useful, it is more advantageous to summarize the information by finding compositionally distinct combinations of these elements. To find these unique constituents, the data were first processed using DTSA II to convert the x-ray spectral data into compositional data[30] through the use of a suite of pure elemental and mixed compositional standards. Then, multivariate statistical analysis was performed on the data to reduce it to a few high variability vectors[31]. While many data transformations exist that can provide unsupervised classification (e.g., k-means, principle component analysis, or agglomerative nesting, etc.), the scheme chosen was known as ISO Means, and is part of the hyperspectral analysis program called ENVI[32]. The ISO means method uses principle components and k-means clustering in addition to in-class statistical controls to identify compositionally distinct areas. Pixels with high variability were separated out into an “unclassified” group. Subsequent analysis of “unclassified” pixels indicates that the high variability on some samples was due to high surface topography. It should be noted that larger fly ash particles are far more likely to contain large air bubbles, which, when cross sectioned, show up as sizeable depressions in the images and

unclassifiable pixels. Therefore, unclassified regions should reduce on smaller or more homogeneous phases.

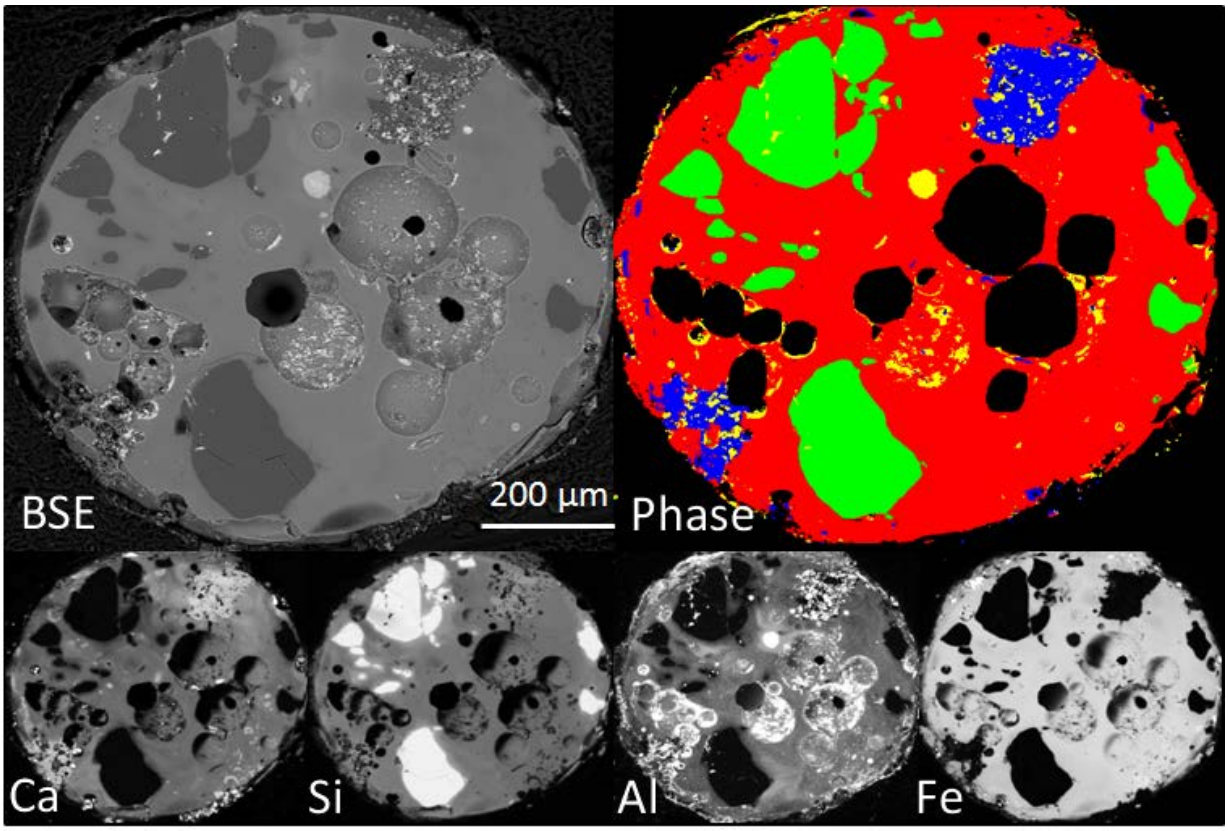

Figure 32: The gray scale images shows the backscatter and elemental maps from EPMA for particle 1C. The segmented constituent phase analysis used in TACCo is shown in the upper right.

This classification scheme has dual purposes; first, it seeks to separate out the constituents of highest compositional variance so that a comparison can be made to the µCT data; second, it allows an estimate of the compositional variance to be determined. The results from this segmentation can be seen in Figure30c and 32.

Fusing Electron Probe Microanalysis and micro Computed Tomography Datasets

A novel software algorithm was created that uses the EPMA data to find the matching plane in the 3D tomography data. This algorithm solves a 14 degree of freedom (DOF) optimization problem that finds the location, rotation angle, scaling, and determines the topology of the polished surface of the sample by using eight different localized planes to match the datasets. A reconstruction of the polishing plane is shown in Fig. 1d and the matching plane is shown in Figure30e. The matches are determined

by comparing binary images from the EPMA and μCT data sets and minimizing their difference. Figure30f shows the result of an overlay for a typical sample.

The accuracy of the match is determined by comparing the coordinates of feature specific pixels. If the compared features in both EPMA and □CT were fo same normalized coordinate then it is considered to be a good match. The matching accuracy is estimated by the number of matched pixels divided by the total number of feature specific pixels compared.

Segmentation of the micro Computed Tomography Data

The correlation between μCT and EPMA now provides the user with guidance on which gray scale values in the μCT correspond to the chemical constituents in the fly ash. Now that the data has been fused, a comparison can be made between the gray scale values of each constituent phase and their frequency. This allows the range of gray scale values to be determined for each constituent.

To help resolve the overlap between the materials, the mean and standard deviation of each constituent was determined for the cross section, and then these values were projected onto the gray value versus frequency plot for the entire particle. The constituent with the highest frequency was examined first. If there was a constituent with gray values adjacent to the high frequency material, then the limit of that phase was taken as one standard deviation away from the mean in the direction of the overlap. If there was no adjacent constituent phase, then two standard deviations away from the mean was used as the limit. The two standard deviation limit was only used when establishing the boundary between the matrix phases and the high absorption phases. This process was completed for each of the phases in their order of appearance. In some cases, there was significant overlap between the minor phases. These areas of high overlap ranges were defined as a mixture.

Particle 1C contained the most voids of the particles investigated and so was used to determine the limits of the gas phase. This established limit was then used for the other particles. Because of the consistent instrument and reconstruction settings used, a standard value for all of the particles was used.

Analysis of 3D Constituent Data

After establishing the segmentation ranges for each constituent this data can be used to create 3D data sets. An example for Particle 1C is shown in Figure 33 with a quarter of the particle removed. This 3D data can be used to find the quantity and distribution of these constituents within a particle. This information is important as not

all constituents have the same chemical reactivity or solubility. This means that a particle may be a more effective binder if key phases are concentrated near the surface.

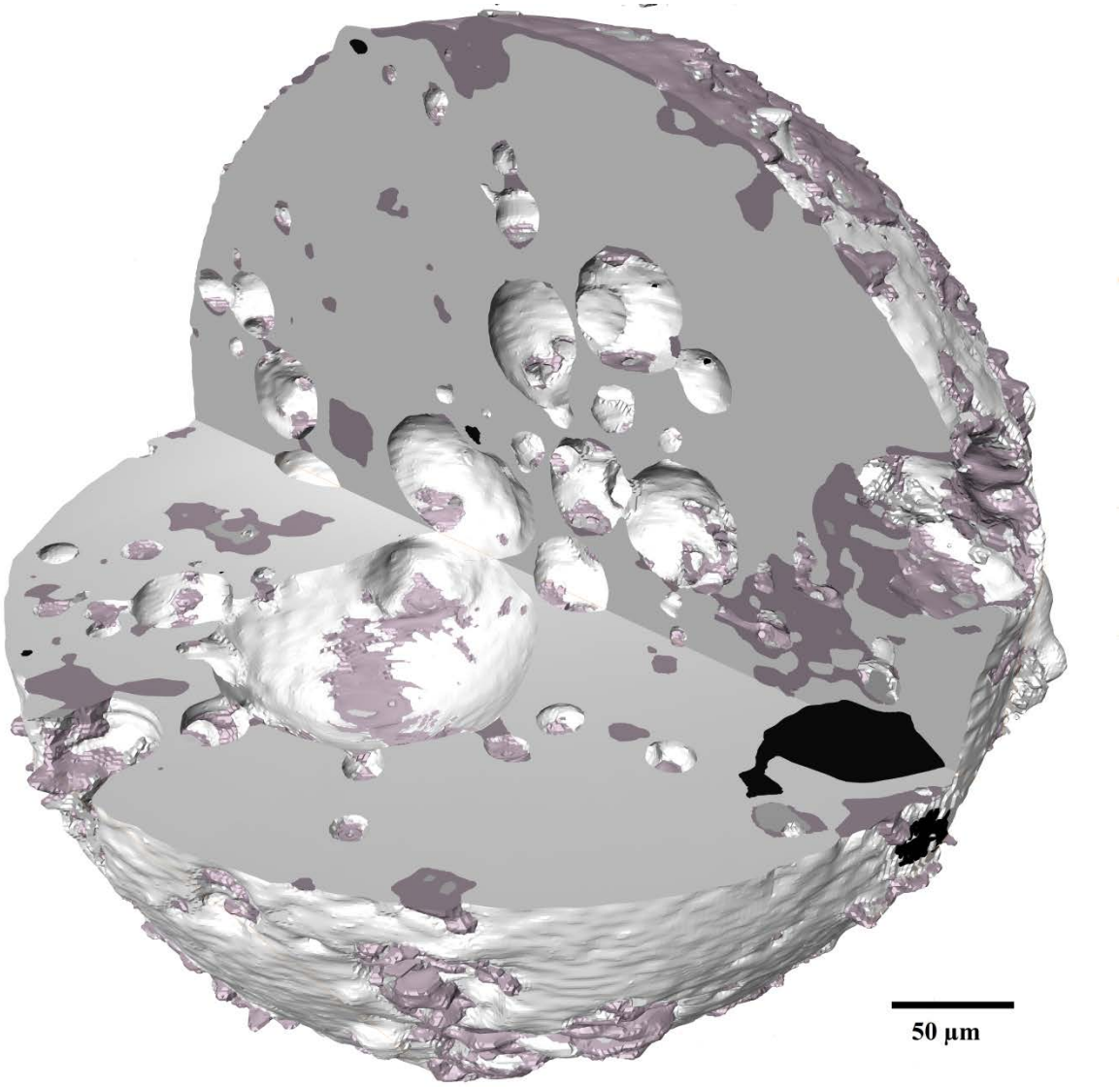

Figure 33: A 3D model of the segmented µCT data. One quadrant of the material has been removed so that it is easier to view the distribution of constituents within the particle.

A novel software algorithm was authored that analytically peels the particle into 1 µm layers or shells of uniform thickness that are parallel to the particles outside surface as shown in Figure 34. For each of these layers, the percentage of each constituent is found as well as the distance from the centroid. Since fly ash particles are largely spherical, data can be produced that shows the concentration of these constituents with depth from the surface. Because of border averaging and phase contrasts, the first 8 µm of the data was not included. Methods to better characterize this surface data will be investigated in future work.

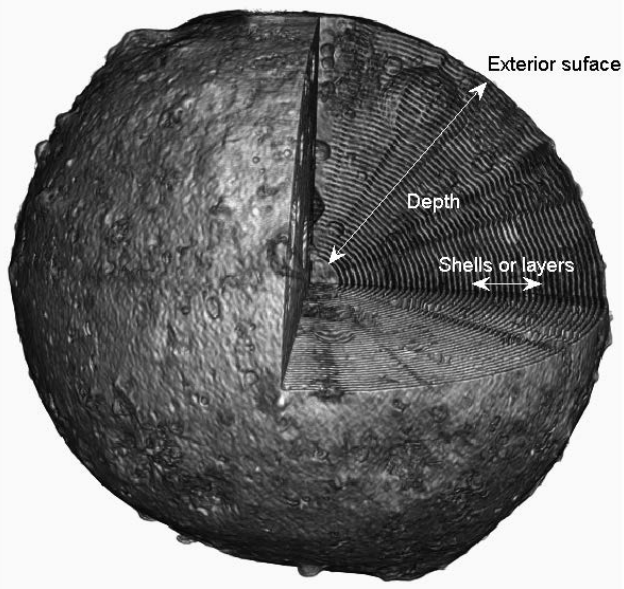

Figure 34: Shells or layers with 1 μm uniform thickness parallel to the particle surface were analytically peeled from exterior surface at different depths.

Results

Micro-Computed Tomography

A graph of the number of voxels for a particle at each gray scale is shown in Figure 31 for sample 1C. As discussed previously, the gray scale value measured is an indication of the density and the mass absorption coefficient of the constituent material. The initial peak in the histogram corresponds to the gas found in the voids. The peak at gray value 255 is a high absorption material associated with metals. Two peaks near gray values of 50 and 100 can also be seen. This suggests that there are at least three major constituent phases that make up the particle. Some constituent peaks show some overlap; this can be complicated by the presence of minor phases or density irregularity within each phase. These naturally complex materials are a good test for the TACCo method to elucidate what phases can be separated.

Electron Probe Microanalysis

The images derived from the EPMA data for Particle 1C are shown in Figure 32. The back scatter, maps of the primary elements, and then the results of the chemical segmentation are given. A summary of the chemical phases found are included in Table 12. A color has been given to each unique phase. The weight percentage is given for each element, as well as the percentage on the cross section investigated, and the calculated mass absorption coefficient. The mass absorption was calculated from the elemental makeup and by using NIST X-ray Attenuation Databases[33]. A

ternary diagram for calcium, silicon, and aluminum is plotted in Figure 35. The ternary diagram shows that nine different chemical constituents were identified.

Table 12 – Summary of the Different Compositions Observed with the EPMA.

element		Ca	Si	Al	Fe	O	K	Mg	S	Ti	area % on cross section	mass absorption coef* (cm^2/g)
Particle 1C - 427 µm diameter												
yellow	weight %	9.66	10.10	6.72	67.17	3.56	0.34	1.31	0.47	0.67	2.52	6.50
	1σ	7.05	6.64	4.62	12.46	6.12	0.51	1.61	0.93	0.97		
red	weight %	27.87	22.96	12.38	10.88	20.00	0.32	3.19	0.55	1.86	70.60	2.76
	1σ	6.78	5.90	3.49	7.87	9.98	0.46	1.68	0.61	1.12		
blue	weight %	4.36	29.35	31.00	14.59	19.11	0.35	0.56	0.27	0.41	5.82	2.15
	1σ	6.69	8.81	8.40	13.75	12.09	0.64	1.22	0.47	0.69		
green	weight %	1.08	65.21	0.53	1.29	31.29	0.07	0.17	0.12	0.26	21.05	1.09
	1σ	2.70	7.22	1.10	2.99	6.67	0.33	0.34	0.25	0.56		
Particle 2C - 427 µm diameter												
cyan	weight %	12.54	32.83	12.27	8.25	26.97	3.47	1.47	0.42	1.78	5.23	3.57
	1σ	5.40	9.78	5.99	6.87	9.88	2.02	0.93	0.63	2.10		
red	weight %	24.99	19.94	11.69	12.67	24.00	0.69	3.15	0.99	1.88	83.51	2.73
	1σ	6.56	4.87	2.78	5.26	10.01	0.59	1.07	1.11	1.06		
peach	weight %	15.24	11.50	14.12	28.64	21.05	0.63	6.00	1.39	1.43	6.09	2.44
	1σ	4.99	4.83	4.89	13.20	10.42	0.61	2.71	1.37	1.06		
gray	weight %	21.02	13.33	24.50	10.22	20.72	0.82	2.12	5.82	1.44	0.73	2.09
	1σ	14.34	9.90	14.26	7.74	13.33	0.82	1.86	8.35	1.66		
green	weight %	3.47	58.98	1.81	3.58	30.43	0.34	0.42	0.35	0.62	4.44	1.08
	1σ	3.88	9.99	1.93	4.46	8.91	0.55	0.50	0.74	1.15		
Particle 4C - 615 µm diameter												
Forest Green	weight %	19.94	51.22	9.64	7.06	5.50	2.23	2.21	0.48	1.71	0.61	2.54
	1σ	12.44	16.12	4.79	4.81	7.90	1.85	1.53	0.57	1.24		
red	weight %	21.69	26.69	10.16	6.39	29.77	0.62	3.12	0.19	1.36	88.10	2.16
	1σ	3.40	3.59	1.56	2.38	6.73	0.44	0.60	0.22	0.66		
brown	weight %	6.56	36.42	15.08	3.81	33.30	2.54	0.93	0.17	1.19	3.47	1.70
	1σ	4.97	8.03	6.72	5.70	8.76	1.19	0.75	0.22	0.88		
purple	weight %	18.82	27.55	18.86	3.41	29.41	0.26	0.99	0.16	0.54	1.54	1.34
	1σ	4.22	3.40	3.25	1.68	7.28	0.35	0.56	0.23	0.51		
green	weight %	1.55	56.17	1.42	1.23	38.52	0.37	0.26	0.13	0.35	6.29	1.00
	1σ	2.44	6.85	1.67	2.20	5.90	0.63	0.37	0.18	0.53		

*These values have been calculated based on the chemical makeup of the constituent by using NIST X-ray attenutation databases

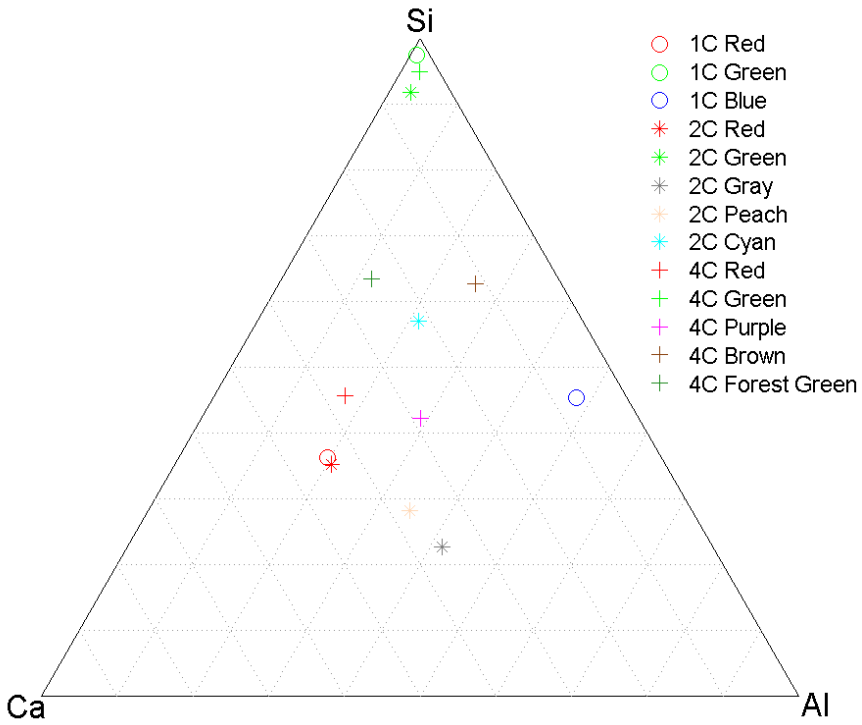

Figure 35:A ternary diagram for the Si, Ca and Al composition for different unique constituents.

The red and green constituents were found to be the major constituents in each particle investigated. In all three particles the red phase was found to be made up of approximately 20% calcium, silicon, and oxygen with aluminum and iron at 10% and trace amounts of magnesium. In all three green phases they were almost entirely silicon and oxygen. While small concentrations of other elements are found in each constituent, the standard deviation was found to be the magnitude as the mean for the element and so not statistically significant. This suggests that some of these elements may be present but are not a fundamental element in that constituent.

Data Fusion

An overlay of the EPMA and μCT is shown in Fig. 30f. At each pixel the gray value and the corresponding constituent phase is recorded and the number of observations at each gray value is plotted in Figure 36. The top plot shows the total number of observed pixels at each gray value for the different constituent phases from the overlay of the cross sections from the EPMA and μCT. The color of each line is indicated by the corresponding color from the EPMA segmented image. Also the mean is shown by a solid line and the standard deviation is shown as a dashed line. For the

red phase two standard deviations is also shown towards the high absorption material as a line with finer dashes.

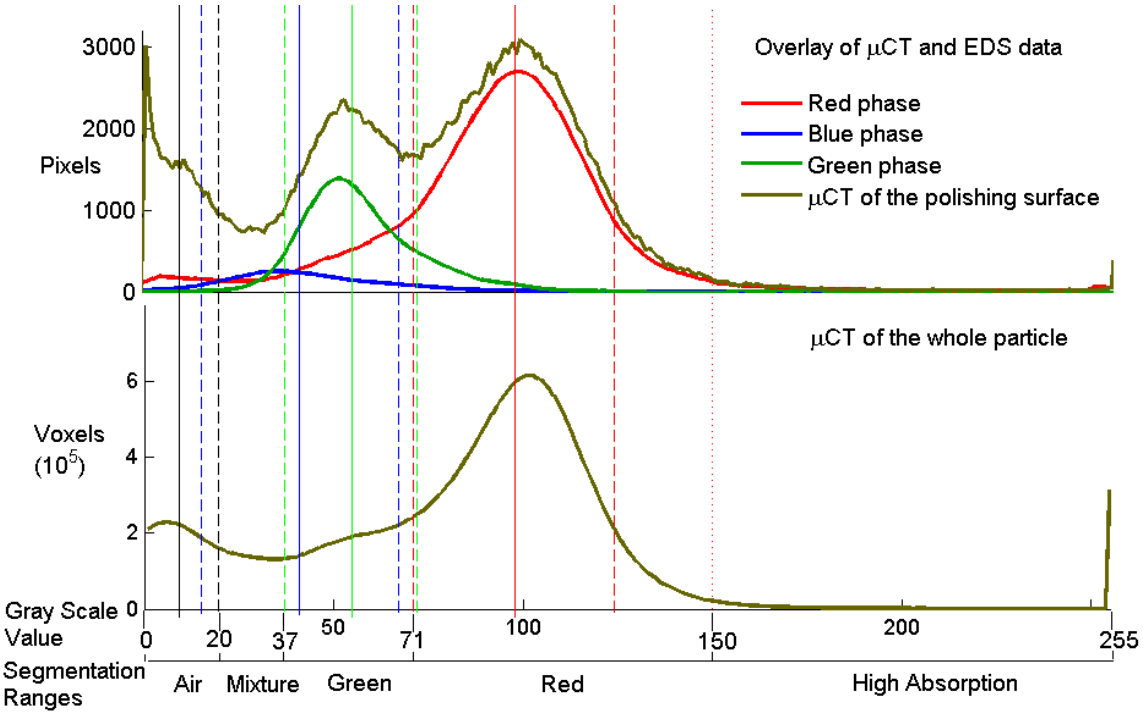

Figure 36: A comparison of the EPMA and μCT data. The top plot shows the number of pixels versus the gray scale value from the data sets. The mean is shown as a solid line and the standard deviation as a dashed line. The bottom plot shows the number of voxels versus gray scale for the entire particle with the projected mean and standard deviations.

The lower plot of Figure 36 shows the voxel distribution. The x-axis of these two plots is aligned and the mean and standard deviation have been extended so that these values can be compared in both plots. Again, the line colors correspond to the labels of the constituents from the EPMA analysis.

Table 13 –Summary of the mean and standard deviations of all the phases.

Phases		Particle name		
		1C	2C	4C
Red	Mean	98	103	99
	1σ	27	21	18
Green	Mean	55	76	63
	1σ	17	24	28
Air	Mean	10	10	10
	1σ	10	10	10
Blue	Mean	41		
	1σ	26		
Cyan	Mean		87	
	1σ		23	
Peach	Mean		109	
	1σ		24	
Brown	Mean			60
	1σ			34

The segmentation decisions are based on the scheme mentioned previously. A summary of the means and standard deviations is given in Table 13 for particle and phase. After establishing the limits for each phase the results are given in Figure 37. For Particle 1C the limits for the red phase were found to be between a gray value of 150 and 71. This is two standard deviations from the mean towards the high absorption phase and one standard deviation towards the overlapping constituents. Next the air phase was established to be a gray value of 20. This is one standard deviation from the mean. The green phase was taken to be values between 71 and 37. The 37 was chosen as it was one standard deviation from the mean towards the overlap and the 71 limit was established from the red constituent. The remaining gray values between 20 and 37 will be treated as a mixture.

Figure 37 – Summary of segmentation ranges for three particles.

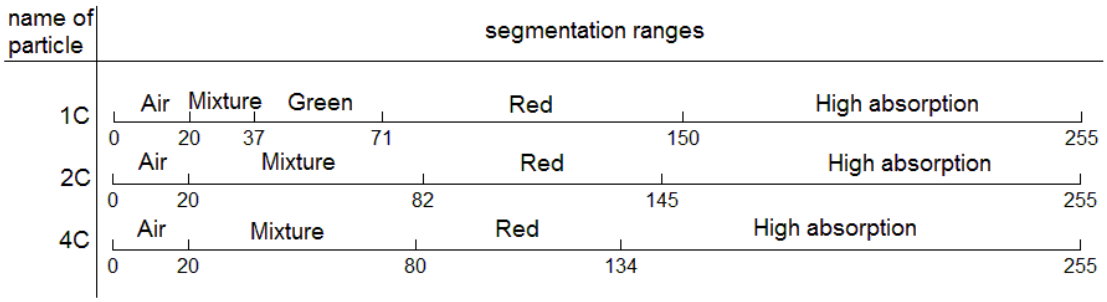

3D Data Analysis

Figure 33 shows the segmented 3D data set for Particle 1C. Colors in this image have been changed to improve the data presentation. The gray, purple, dark gray and black correspond to the red, green, mixture and high absorption constituent phases respectively. The peel algorithm is then used to find the distribution of the phases within Particle 1C. Results are shown in Figure 38. In this plot the y-axis shows the percentage of the constituent present versus the depth from the outside surface. Since fly ash particles are spherical in nature, these thicknesses go from the particle surface towards the center. This data shows how the constituent concentrations change over the particle diameter.

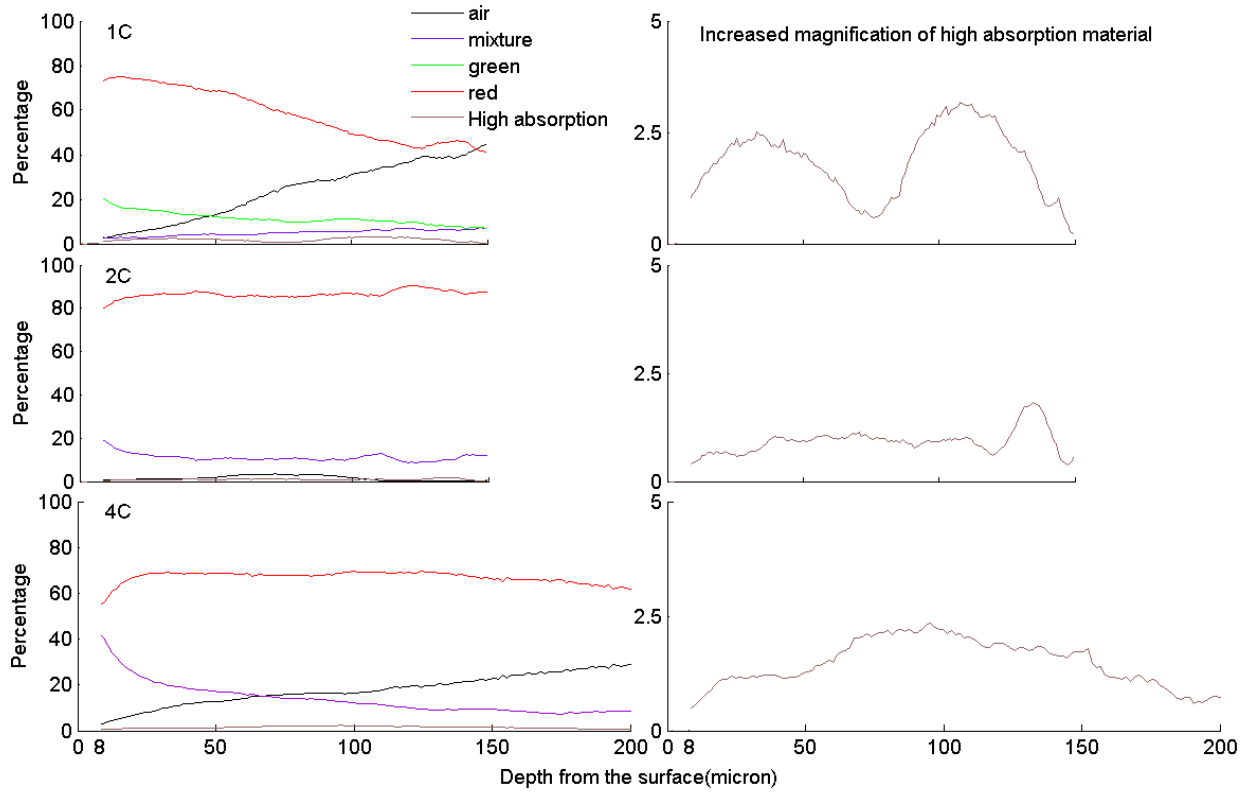

Figure 38: A plot of the percentage of each of the segmented phases within the 3D particle versus the distance from the centroid of the particle.

Discussion

Micro computed tomography is a powerful nondestructive 3D analysis technique that is widely used in the medical sciences. The gray values from these measurements are an indication of the mass absorption and density of the material. It is not currently possible to directly use these gray values to indicate the chemistry of a material unless it is a very simple sample. For example in Figure 31 it is possible to determine that gas, a high absorption, and at least two other constituents exist but it is challenging to

determine their limits for gray scale segmentation. Also it is not possible to determine the compositional makeup of these constituents. The TACCo technique is able to overcome these limitations and allow for a more thorough segmentation from μCT data.

Repeatability of the Method

TACCo was used on three different particles from the same source of fly ash. The data in Table 12 and Figure 34 show that the compositional makeup for the red and green phase was consistent. Consistency was also found in the fused data sets, as the mean and standard deviation of these constituents, as shown in Table 4, were similar for both the red and green constituent. The fusion data for the other constituents did not match, but this is expected as they are unique compositional phases. Finally, the ranges given in Figure 37 for the final segmentation of the particles were also similar. In Particle 1C, it was possible to determine a range of gray values for the green phase. However, this was not possible for the others, because there was too much overlap of the gray values in the minor phases. Further segmenting these minor phases will be examined in future work.

Compositional Makeup of Fly Ash

The EPMA data allows powerful observations of the compositional makeup of these complex fly ash particles. While differences in the minor constituents were observed, the red and green constituents were found in each of the three particles investigated and consist of over 90% of the cross sections investigated with the EPMA as outlined in Table 12. The red constituent was the most prevalent observed in the particles as it was never less than 45% of the volume of a particle and regularly greater than 75% of the volume.

Chemical Consistency with Depth

The strength of TACCo is that it can observe the compositional consistency over the depth as shown in Figure 38. This information about the uniformity is helpful to understand the chemical reactivity of the particle with depth. Of the three particles investigated, Particle 2C was found to be consistent in all constituents over the depth. The other particles were found to change with their depth as described below.

Particle 1C had the greatest volume of gas. The gas increased with depth and the red and green constituent decreased. The green constituent decreased until about 75 μm from the surface and then stayed approximately constant. The mixture stayed at a constant concentration in the particle. The high absorption constituent showed increased concentrations at 35 μm and 120 μm from the surface. This seems to be unique to this particle.

In Particle 4C a high concentration of the mixture was observed at the surface and then decreased with depth. As the mixture decreased, the red and gas phase increased until 20 μm from the surface. After 20 μm the red phase stayed constant as the mixture continued to decrease and the gas increased. The high absorption phase was found to increase from the surface until 90 μm and then decrease.

Summary

This chapter has presented a new analytical technique, Tomography Assisted Chemical Correlation (TACCo). TACCo was shown to create 3D chemical maps of complicated materials by combining EPMA and μCT on the same sample. By fusing this data, a calibration is made that helps guide the segmentation of the μCT data to produce 3D constituent maps of the microstructure. From the particles investigated, the following statements can be made:

- The technique was demonstrated to perform consistently on three different fly ash particles from the same source.
- The technique found that there were two unique constituents that made up over 50% of the volume of the particles. Minor phases in the particles were observed as well.
- The segmentation ranges for these repeated constituents were similar between particles.
- 3D chemical models were created for the fly ash particles.
- The subsequent analysis of these 3D models showed that, while there was similarity between the constituents in each, the chemical distribution with depth differed.

TACCo is unique because it has the ability to create detailed 3D chemical maps of materials regardless of whether they are crystalline or amorphous. As X-ray techniques continue to improve, the resolution and capabilities of TACCo also improves. With existing laboratory instrumentation, the data produced is already useful and has the ability to give great insight into important materials.

In this work a calibration was needed to fuse the EPMA and μCT data. After this calibration has been established on a number of particles, then these same gray value ranges can be used for future particles. This will allow subsequent similar particles to be compositionally investigated only using μCT. This allows a larger number of particles to be scanned simultaneously, segmented by gray scale, and then subsequently investigated with the peel algorithm. With the present equipment, an 8 mm high scan can be performed with a 1 μm resolution in the same sample chamber, and since there are no size constraints to this method, hundreds of particles can be

scanned at once. This technique now becomes an outstanding tool for many applications where a large number of particles need to be rapidly characterized.

After establishing the composition associated with an absorption range it is also possible to create a 3D chemical map of a complex particle and then subject it to a solution and then create a new 3D chemical map to determine the changes to the particle. Since the μCT technique is nondestructive it is possible to continue to use the same sample and image subsequent changes. Because the initial gray value is known the compositional content would also be known. Any changes to the volume, density, or compositional consistency can also be imaged. This creates a 5D set of observations to be made. This includes changes in spatial location, compositional consistency, and time. These observations can provide critical in *situ* measurements of how complex materials react in different solutions.

CHAPTER 4 - PHYSICAL TESTING

For the determination of the physical properties, three experiments were conducted on hardened concrete mixtures containing 20% fly ash by weight as cement substitute. The results obtained from these experiments were compared to a final concrete mixture which consisted purely of straight Portland cement as its sole cementitous media. The experiments that were conducted on these mixtures were as follows: a compressive strength test on a standard concrete cylindrical specimen 4 inches in diameter and 8 inches in height (ASTM C39)[34], the monitoring the length change of concrete prisms due to forcing an Alkali-Silica reaction to take place (ASTM C1293)[35], and the determination of the chloride diffusion coefficient of the different concrete mixtures based on the bulk diffusion theory (ASTM C1556)[36]. These tests were done in addition to typical fresh concrete property testing, such as the fresh density test of the concrete (ASTM C138), slump test (ASTM C143), and air content within the concrete mixture using a pressure gauge (ASTM C231). Table 14 contains the main cement oxide chemical contents and its corresponding phase composition for the two different cements adopted within this project. These phase compositions were estimated based on Bogue calculations. In Table 14, the first cement is type I that has been used for testing ASTM C39 and ASTM C1556, while the second is a special type of cement that has been used for testing ASTM C1293 specifically.

Table 14 - Chemical composition of the cement adopted

	Used in : ASTM C39 & C1556	Used in: ASTM C1293
	Cement Type I Bulk XRF Oxide Composition	
SiO_2 (%)	20.4	19.27
Al_2O_3 (%)	5.03	6.11
Fe_2O_3 (%)	2.95	2.09
CaO (%)	62.89	62.34
MgO (%)	2.08	2.59
SO_3 (%)	3.05	3.87
Na_2O (%)	0.35	0.21
K_2O (%)	0.35	1.28
Na_2O equivalent	0.58	1.05
	Cement Type I Phase Mass Composition based on Bogue calculation	
C_3S (%)	62.92	63.25
C_2S (%)	11.09	7.59
C_3A (%)	8.34	12.66
C_4AF (%)	8.98	6.36

As seen in Table 14, two distinctly different cements were adopted in this project where the total alkali content of both cements was 0.58% and 1.05% consecutively. Based upon this chemical composition, the special cement was used for testing the ASR mechanism do to its high Na_2O equivalent.

The concrete mixture design used in this project is listed Tables 15 and 16. Both Tables contain the different mixture conducted to ensure the success of the project scope for all sets of experiments as mentioned earlier. Table 15 mixtures were used in ASTM C39 and ASTM C1556, while Table 16 mixtures were used in ASTM C1293. In Tables 15 and 16, the batches for any of the five fly ashes' concretes were identical compared to the straight Portland cement concrete where a slight adjustment in batch weights had to be compensated for in order to accommodate the volumetric changes and maintain the w/cm ratio at 0.45.

Table 15 - Mix Proportion Used in ASTM C39 & C1556

	Cement (lb/yd^3)	FA (lb/yd^3)	Coarse Ag. (lb/yd^3)	Fine Ag. (lb/yd^3)	Water (lb/yd^3)	w/cm
Typical Fly Ash Mix	489	122	1850	1203	275	0.45
Portland Cement Mix	611	-	1860	1215	275	0.45

Table 16 - Mix Proportion Used in ASTM C1293

	Cement (lb/yd^3)	FA (lb/yd^3)	Coarse Ag. (lb/yd^3)	Fine Ag. (lb/yd^3)	Water (lb/yd^3)	w/cm
Typical Fly Ash Mix	566.4	141.6	1917	953.4	318.6	0.45
Portland Cement Mix	708	-	1917	963	318.6	0.45

Fresh concrete testing

Fresh concrete tests are important practices because they indicate the subsequent performance in hardened concrete testing. They directly relate to the concrete sampling in addition to its potential regarding both strength and durability. The fresh concrete test methods were adopted in such a manner in order to determine the consistency and workability of the different mixture by using the slump test following the specifications in ASTM C143, determining the fresh density following the specifications in ASTM C138 and determining the air content by the pressure gauge method following the specifications in ASTM C231. The following Table 17 offers the output for the three fresh testing criteria for the five different mixtures in addition to the control mixture.

Table 17 - Fresh Concrete properties

	Slump (in)	Air Content (%)	Unit Weight (lbs/ft^3)
C1	6.5	1.80	148.00
F	5.5	1.80	147.76
C2	6.0	1.60	148.56
C3	6.5	1.40	148.80
C/F	7.0	1.80	147.84
Portland Cement	3.0	2.10	146.49

As mentioned earlier, 20% of the cement within the mixtures was substituted by fly ash; this substitution helped sufficiently in improving the workability of the concrete mixtures.

Harden concrete testing

ASTM C39 - Compressive Strength

In order to measure the impact of the different fly ash on the strength of concrete mixtures, ASTM C39 compressive testing was conducted on 4 inch x 8 inch cylinders prepared from the six concrete batches mentioned earlier. For each mixture, 24 cylinders were prepared and three of those cylinders were tested and evaluated at 3, 7, 14, 28, 56, 90, 180, and 365 days consecutively. Figure 39 shows the results from compressive testing up to the first 28 days corresponding to the early age performance of the 6 concrete mixtures. The error bar shown in the Figure displays a single standard of deviation.

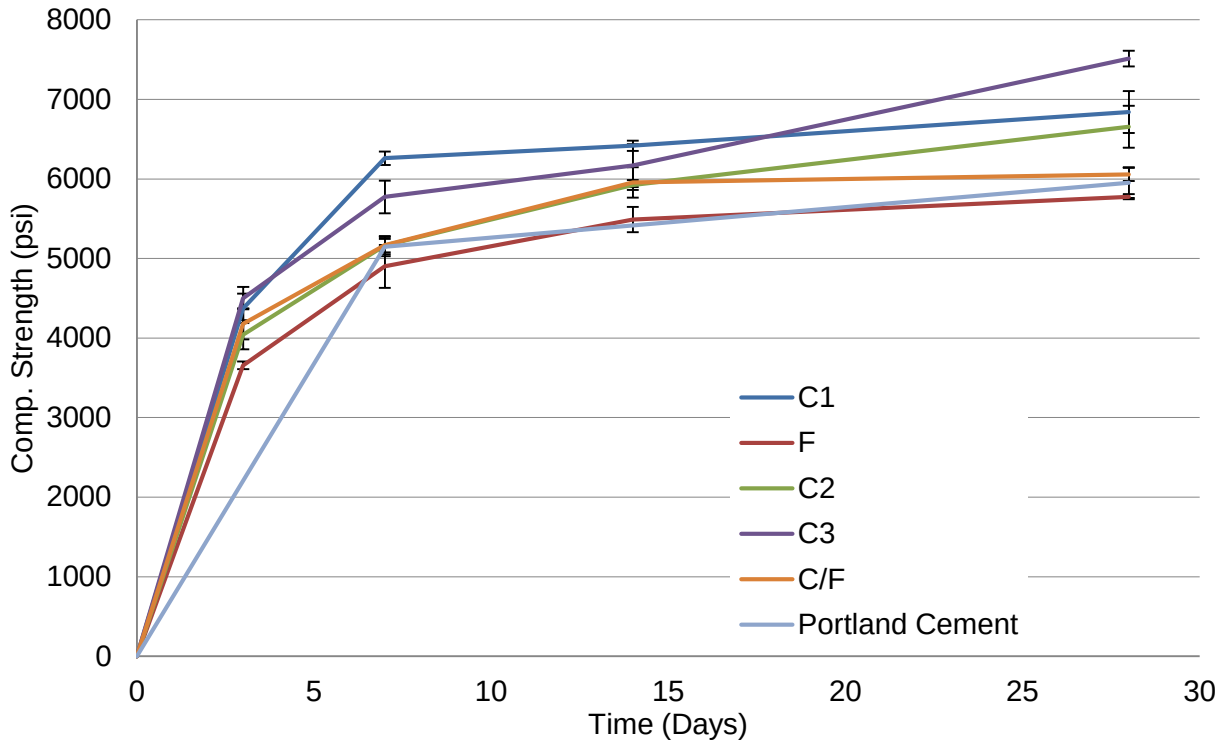

Figure 39: The relationship between compressive strength and the type of fly ash over the first 28 days.

The average compressive strength data was collected at 3, 7, 14 and 28 days from three specimens per age per concrete mix were tested as seen in Figure 39. It

can be observed that two distinct groups were observed by the end of the 28th day. The first group consisted of all three class C fly ash with an average compressive strength exceeding 6500 psi for each of the mixtures. The second group consists of the other fly ashes, F and C/F, in addition to the straight Portland cement mixture, with an average compressive strength lower than 6000 psi at the 28th day. This supports the known concept that class C fly ashes help in increasing the early age strength of concrete mixtures. Figure 40 graphically illustrates the average compressive strengths of each of the six mixtures at designated day of testing from age 3 days up to 365 days in addition to a single standard of deviation.

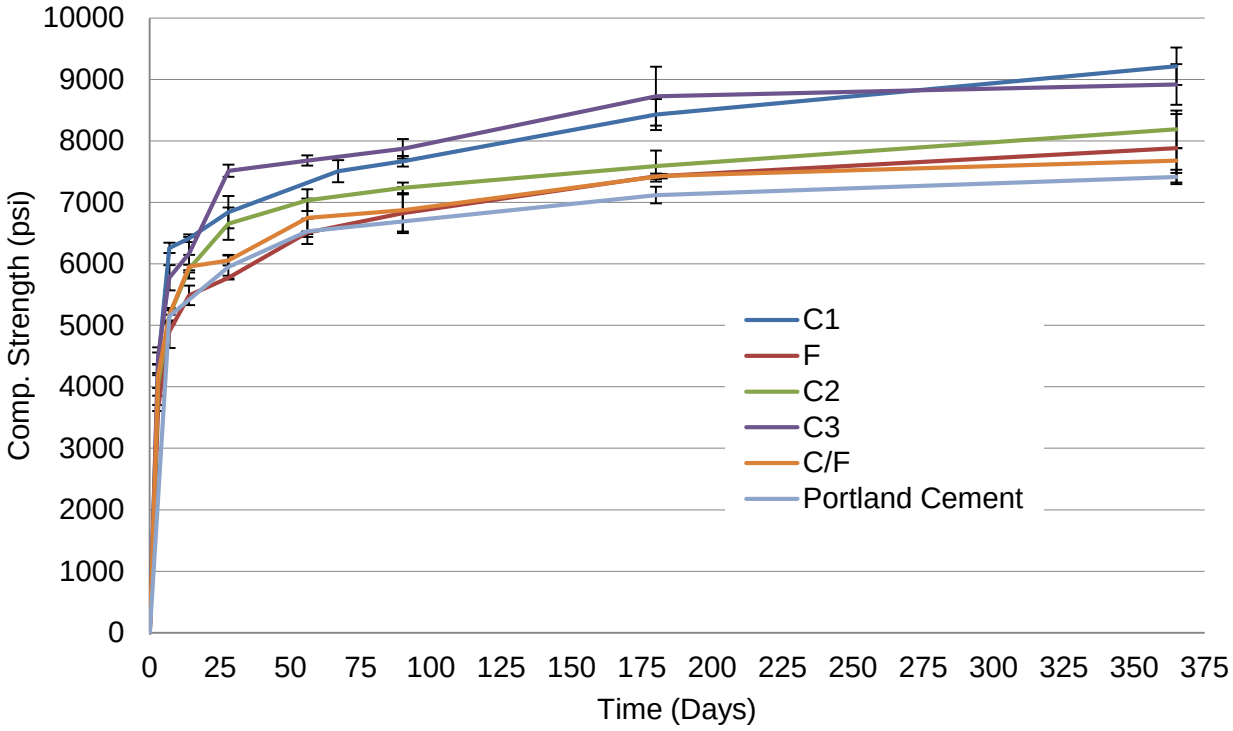

Figure 40: The relationship between the compressive strength and the type of fly ash.

From Figure 40 it seems that all mixtures containing class C fly ash had a superior performance at later ages similar to earlier ages, where after one year all three concrete mixes containing class C fly ash had a strength exceeding 8000 psi. Comparatively, strengths of the F concrete mix and C/F concrete mix were limited to 7881 psi and 7682 psi consecutively, while the control straight cement concrete mixture had a compressive strength of 7415 psi for one year old concrete. Figure 40 also suggests that the compressive strength of C1 and C3 had the highest ultimate strength,followed by C2 with a little difference. This higher strength gain for class C fly ash could be attributed to the self-cementing criteria which class F lacks. The secondary pozzolanic reaction of the class F fly ash can be seen as its strength is lower than the Portland cement at early ages and then has superior performance after 60 days.

ASTM C1556 -
Standard test method for determining the apparent chloride diffusion coefficient of cementitious mixtures by bulk diffusion

The chloride diffusion coefficient of concrete can be determined using ASTM C1556. It is a reliable standardized testing procedure that measures the relevant chloride ions transport through a concrete matrix, defining its resisting capabilities against such a diffusing mechanism. Based on Fick's second law of diffusion, it is assumed that the concrete examined during this experiment will remain uncracked, saturated, and constant in density; in addition, it is also assumed that diffusion is the only mass transport mechanism taking place during the chloride ingress in concrete.

Six concrete prismatic in-shape specimens were prepared and cured for each concrete mixture, where the curing period was five days in a sealed environment with a constant temperature of 73 °F. All of the six specimens for the different concrete mixtures were submersed in 165 g/Laqueous sodium chloride solution, which correspond to a weighted percent of 14.16%, for different time settings. The six specimens for each of the mixtures were divided into three groups. The first group was ponded for 45 days, the second group 90 days and the last group for 135 days at a constant temperature of 73 °F. Prior to ponding, specimens were subjected to a precise sample preparation procedure, where the specimen walls were coated with impermeable caulk. Three days later, after the caulk had cured, the specimens were ponded with 3 g/L calcium hydroxide solution for seven days in order to minimize the influence of transport mechanisms other than concentration driven diffusion. At the end of the seven days, the lime rich saturation solution was drained and the samples were rinsed and ready for ponding of sodium chloride.

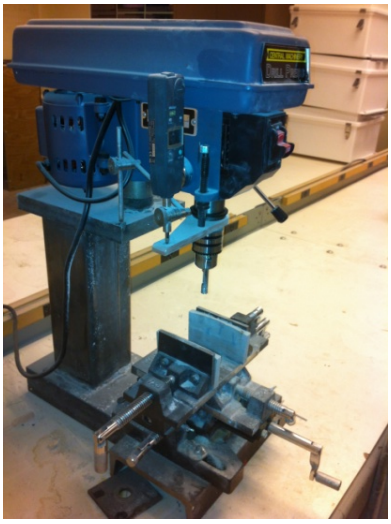

Figure 41: Profile grinding using a drill press with 1 inch core bit

The sodium chloride ponding phase lasted a minimum of 45 days, after which the specimens were immediately rinsed and left to dry for 24 hours under laboratory controlled conditions. At the time of drilling, the samples were drilled in 0.2 inch increments from the top exposed surface up to a depth of 0.8 inch in a chord pattern parallel to the exposed surface using a drill press with a 1 inch core bit seen in Figure 41. The drilling had a minimum length of 3 inches across the desired drilled layer. Four layer depths were used to obtain a 15 g powder sample for each layer of each specimen. Concrete specimen layer depths used are shown in Table 8. After the drilling is conducted, the dust from each level is collected and sieved individually into separate containers. Then the containers are placed in an oven to remove the moisture. Later, the collected dust containers were placed in vacuum sealed desiccators until the titration was completed. The results are shown in Figures 42, 43, and 44. In each of the Figures, the chloride concentration is shown versus the depth for different ponding durations.

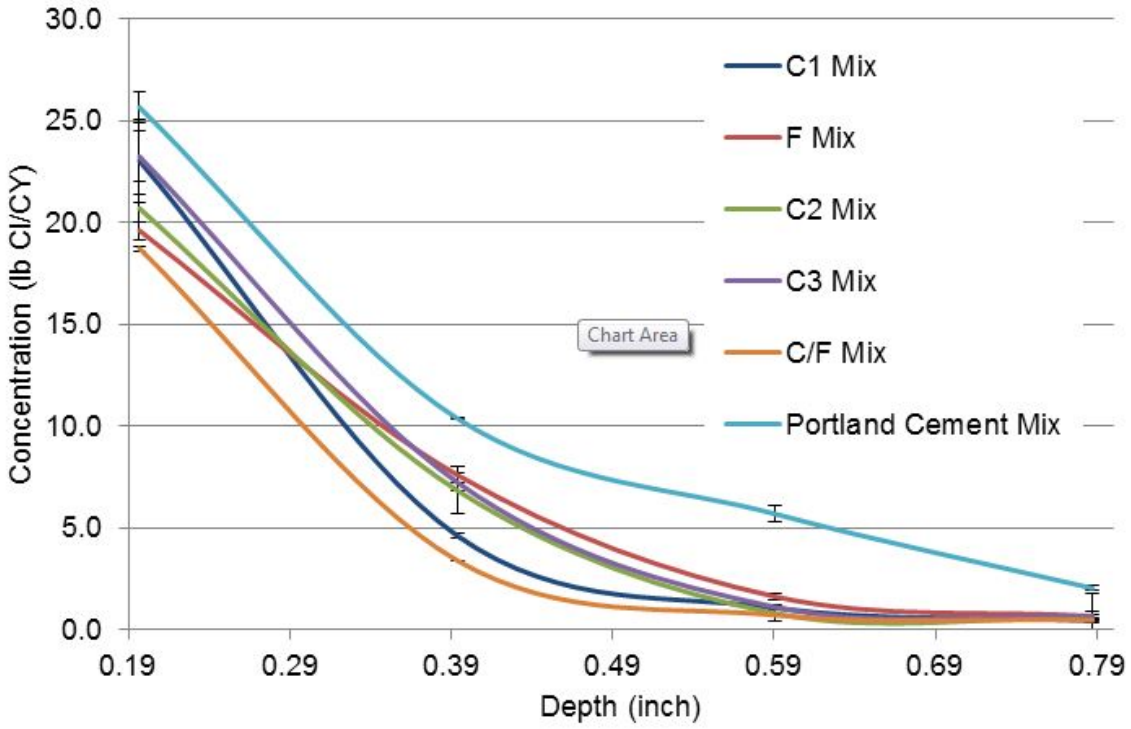

Figure 42: The chloride profile versus depth at 45 days.

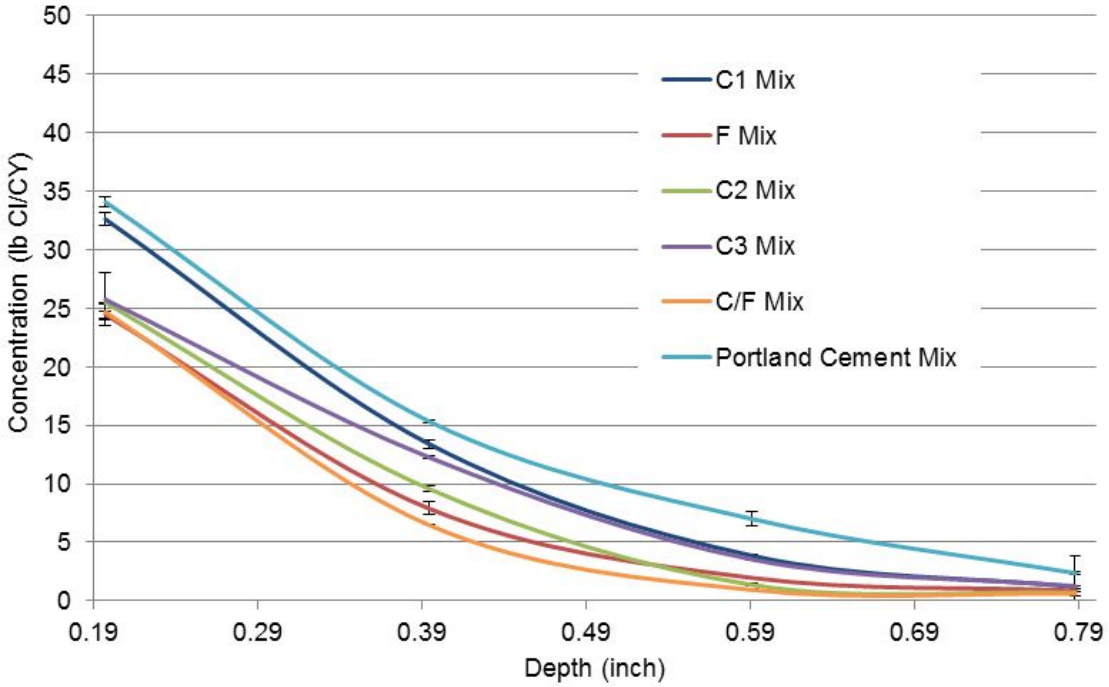

Figure 43: The chloride profile versus depth at 90 days.

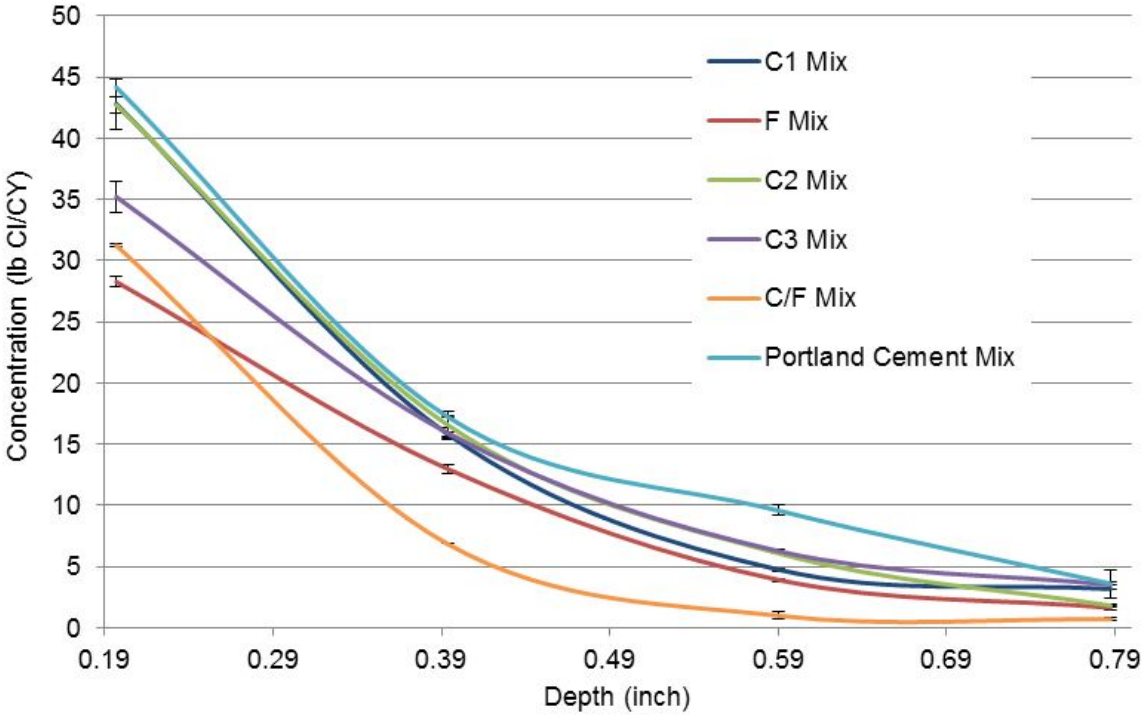

Figure 44: The chloride profile versus depth at 135 days.

From Figure 42, 43, and 44, it seems that the chloride concentration throughout the depth of the concrete must be changing overtime as long as the concrete hydration is taking place. This could be attributed to the decrease in porosity and the network of pores becomes more discontinuous and filled with hydration products.

The clear benefits of using fly ash in concretes can be seen in all three Figures, as all 5 of the commercial types of fly ash have affectively reduced the diffusivity phenomenon occurring at the concrete at the age of 45, 90 and 135 days consecutively by reducing the permeability of the hardened concrete of the fly ash concrete compared to the straight Portland cement concrete. As it seems that C/F had the lowest permeability, this could be attributed to its high alkali content where more chloride ions might have been bounded and blocked from penetrating the concrete. C/F was followed by F in performance. This could be attributed to unique cementitious properties class F possesses in addition to its low alkalinity, allowing more alkalis to be absorbed by the products of the pozzolanic reactions, resulting in the reduction of "free" alkali ions. All of class C had similar performances with higher permeability than the C/F and F fly ashes. Thus it can be seen in Figure 42, 43, and 44, that slower acting pozzolans such as F and C/F ashes attained low long-term chloride diffusion in spite of the early age chloride exposure.

Class C fly ash concrete specimens that were subjected to chloride immersion at 45 days showed a low diffusivity compared to the straight Portland cement mixture. However, with longer ponding, at 90 and 135 days of immersion in solution, diffusivity started increasing and became similar in performance to the straight Portland cement mixture diffusivity at 135 days of chloride immersion. This could be attributed to the fact that at early ages, fly ash is working on clogging the concrete pores and preventing the chlorides from penetrating easily. However, beyond 90 days, the permeability of fly ash concrete increases as the chloride ions found a path through which they easily progress into the concrete.

Finally, class C fly ash improved the diffusivity of concrete compared to mixtures containing only Portland cement, however diffusivity improvements for class C fly ash concretes are much less than the improvements seen with class F and C/F fly ashes.

ASTM C1293 –
Standard Test Method for Determination of Length Change of Concrete due to Alkali-Silica Reaction (ASR)

ASTM C1293 is used to determine the alkali-silica reaction (ASR) taking place in concrete due to the chemical reaction between the reactive silica contained in the aggregates and the alkalis within the cement in the presence of adequate moisture. This

is conducted through monitoring the length change of concrete prisms in a moist environment for two years when fly ash is used. Unfortunately the test data shown is only for one year. However, it is still useful for data comparison. The length change occurs due the ASR. In this phenomenon, an alkali-silicate gel is formed, capable of absorbing water and increasing in volume. This increase in volume would lead to a pressure build up in the concrete matrix causing internal stresses to increase. Once these stresses exceed the allowable tensile strength of the concrete, cracks will start to occur and propagate. Due to the volumetric changes taking place, weight change has been monitored simultaneously with length change.

All the sample preparation and curing was performed in accordance with the ASTM C 1293 specifications. The same types of both coarse and fine aggregates were used in all mixtures. The coarse aggregates were locally available in Oklahoma while the fine aggregates were reactive siliceous sand imported from El Paso, Texas. Concrete prisms that are 3” x 3” x 11 1/8” were prepared in metal molds with embedded pins at its end. After curing, initial measurements were taken, then samples were stored in air tight containers with water at the bottom to keep them at 100^{o}F and close to 100% relative humidity.

During testing, the container holding the specimens should be removed from the oven and left in a moist room for 16 ± 4 hours prior to measuring. Samples were measured at 7 and 14 days and then every month thereafter. Figure 8 shows the results of the testing. Three samples were investigated for each of the reported values. The average and one standard deviation are shown for each data point.

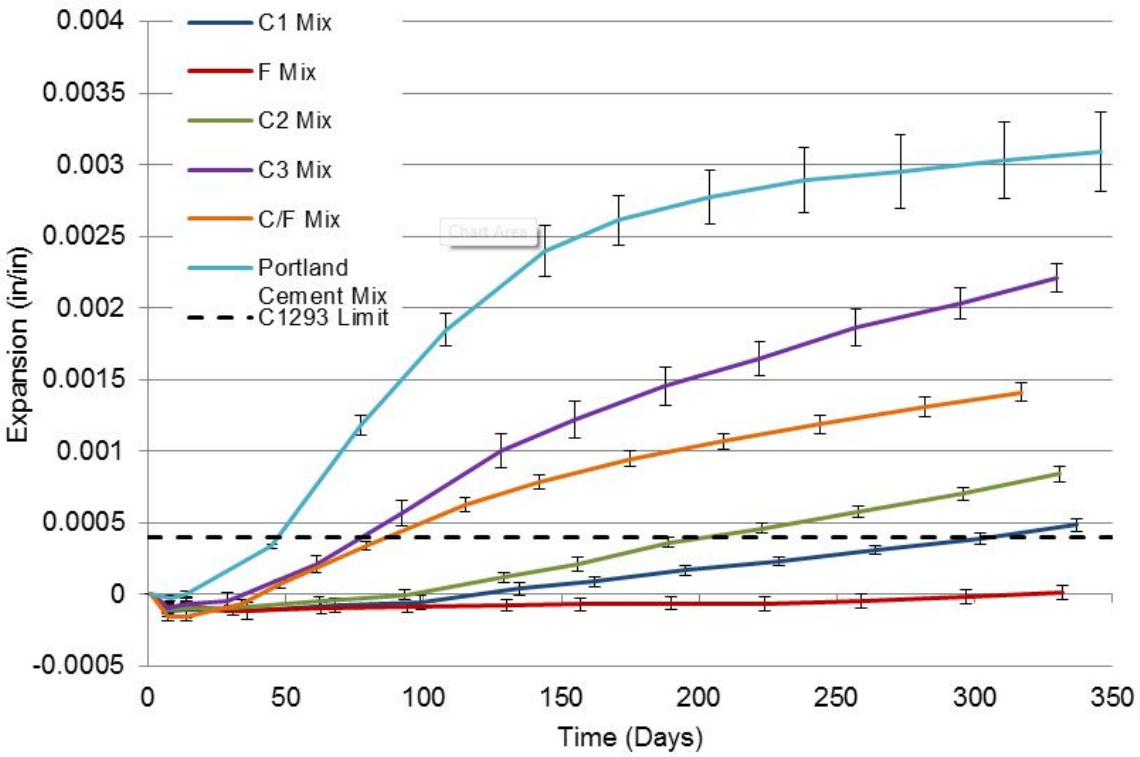

Figure 45: shows the ASR expansion vs Time

Table 18 - The alkali content and Ca/Si for the five commercial types of fly ash

	C1	F1	C2	C3	C/F
Na2O equivalent (%)	2.03	1.45	2.01	1.94	8.39
CaO / SiO_2 Ratio	0.54	0.18	0.66	0.60	0.41
Expansion at 300th day (in/in)	0.00039	-0.00002	0.00071	0.00203	0.00131

From Figure 45 and Table 18, it was found that fly ash in general could be effectively used for reducing concrete expansion; this could be attributed to the reduction in the availability of alkalis within the concrete pore solution due to fly ash addition. Typically, class F fly ashes have superior performance over other types of fly ash due to their high silica content and low calcium and alkali contents; therefore, they are more effective in terms of controlling the alkali available for reaction. It could have been expected the C/F fly ash would have the highest expansion for fly ash concrete mixes due to their very high alkali content; however, this was not the case, as the C3 concrete mix had an even a higher expansion. This could have been due to the non-solubility of these alkalis. The CaO/SiO2 ratio offers another theory, where the lower ratio of CaO/SiO2 in C/F than C3 could have caused C/F fly ash to have a better performance regarding ASR expansion. A lower CaO/SiO_2 ratio might have resulted in more alkali being bound to the hydration products. Consequently, it was found that the

fly ashes with the most silica and the lowest Ca/Si ratio, such as F, and C1, were the most effective in limiting ASR effect in this set of ashes studied.

In Figure 46 it seems that beam performance in ASR testing was significantly reflected on its weight change. The mixtures that were least effected by ASR also had the least changes in weight, which indicates that the relationship between strain gain and weight loss is directly proportional. This is likely due to the microcracks absorbing additional moisture from the humid environment in the buckets.

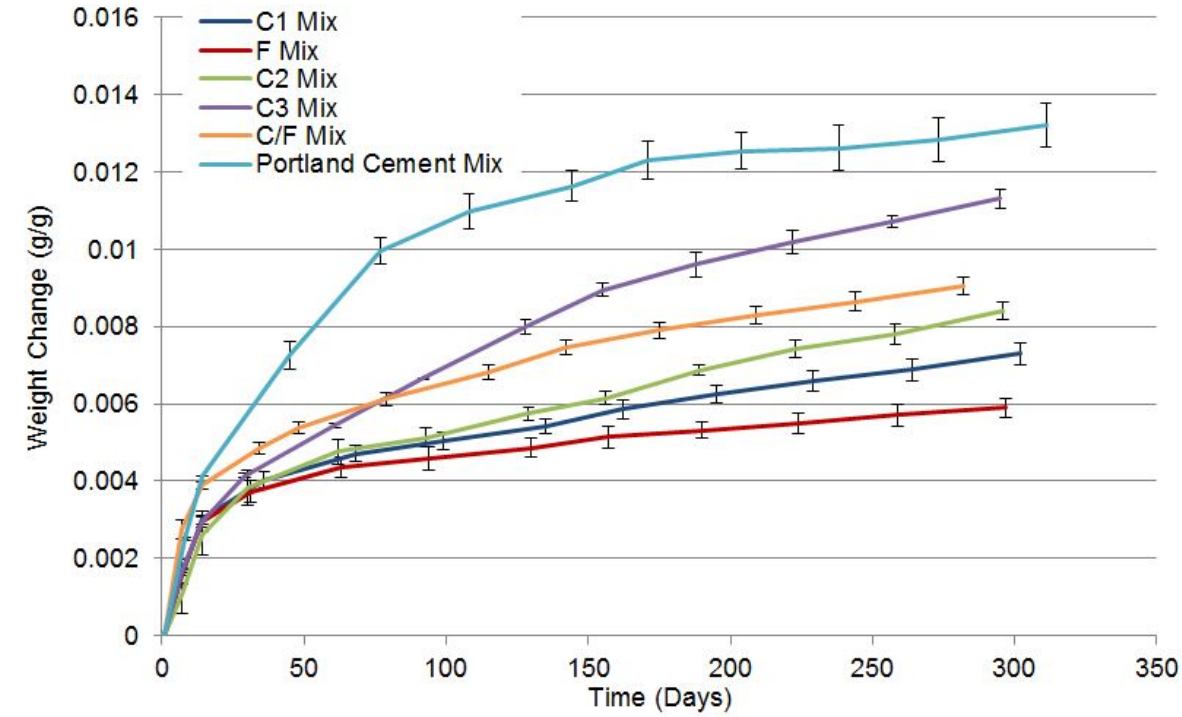

Figure 46: The weight change vs time for the ASTM C 1293 specimens.

Summary

Table 19 offers a summary of the physical testing conducted on harden concrete. The purpose of the coloring system in the table is to quantify different groups and to establish a performance threshold so that different color zones would correspond to different zones of performance of concrete mixtures, where within these selected zones all the concrete mixtures performed similarly to each other in the specific test and testing age addressed. From this table, the green marked zone represented the best performer, yellow represented the intermediate and red represented the lowest performer.

Table 19–Summary for the overall performance and percent difference of all harden physical testing normalized with respect to the control mixture

	ASTM C39				ASTM C1556						ASTM C 1293			
Position	28th Day	% Difference	365th Day	% Difference	45 Days	% Difference	90 Days	% Difference	135 Days	% Difference	Length Change	% Difference	Weight Change	% Difference
1st	C3	26	C1	24	C/F	-65	C/F	-62	C/F	-65	F	-101	F	-55
2nd	C1	15	C3	20	C1	-56	F	-53	F	-44	C1	-87	C1	-45
3rd	C2	12	C2	10	C2	-52	C2	-53	C2	-23	C2	-77	C2	-36
4th	C/F	2	F	6	F	-47	C3	-35	C1	-18	C/F	-57	C/F	-31
5th	SPC	0	C/F	4	C3	-47	C1	-28	C3	-16	C3	-33	C3	-14
6th	F	-3	SPC	0	SPC	0	SPC	0	SPC	0	SPC	0	SPC	0

* SPC = Straight Portland cement

Finally, by observing the results collected from all three harden physical testing performed and conducting a generalized look on the overall performance of the fly ashes it can be concluded that the use of F and C/F fly ashes yield improvements in the concrete performance as compared to the straight Portland cement control mixture. The C1 mixture performed significantly better than the control mixture and other fly ashes integrated within this project. Consequently, C2 and C3 had adequate performance with slight improvements compared to the straight Portland cement control mixture with overall performance lower than F and C/F in rank.

CHAPTER 5 – CONCLUSION

This report has presented the development of two novel particle analysis techniques and a collection of data from the physical testing of concrete containing fly ash. These results show that these techniques show promise for detailed investigation of the mechanisms of fly ash performance. Most notably the TACCO technique has the ability to more fundamentally understand the distribution of phases within fly ash particles, while the ASEM technique provides a statistically robust technique that is able to rapidly investigate a large number of particles. Both of these techniques are powerful and the funding of this project helped establish the validity of both of these methods.

The physical testing chapter clearly shows that despite the bulk chemistry being very similar between the materials investigated, there was a significantly different performance in concrete. The investigation of these materials in detail will provide substantial insights into why these materials perform differently in concrete. Additional work is needed before strong conclusions can be made from this work.

REFERENCES

1. M.R.H. Dunstan, Fly ash as the `fourth ingredient' in concrete mixtures, Fly Ash, Silica Fume, Slag, and Natural Pozzolanics in Concrete, ACI SP-91, Detroit, 1986, pp. 171 ± 197.
2. Ahmaruzzaman, M. A review of the utilization of fly ash. Progress in Energy and Combustion Science 36, 327-363 (2010).
3. Tastan, E. O, Edil, T. B., Benson, C. H. &Aydilek, A. H. Stabilization of Organic Soil with Fly Ash. Journal of Geotechnical and Geoenvironmental Engineering © ASCE, 819-833 (2011, September).
4. ASTMC618, Standard Specification for Coal Fly Ash and Raw or Calcined Natural Pozzolan for Use in Concrete (ASTM International, Pennsylvania 2004).
5. Williams, P.J., Biernacki, J. J, Rawn, C. J, Walker, L., & Bai, J. Microanalytical and Computational Analysis of a Class F Fly Ash. ACI Materials Journal, 102, 330-337 (2005).
6. McCarthy, G. J., Swanson, K. D., Keller, L. P.,& Blatter, W. C. Minerology of western fly ash. Cement and Concrete Research, 14, 471-478 (1984).
7. Winburn, R.S.,Grier, D.G., McCarthy, G.J., & Peterson, R.B. Rietveld quantitative X-ray diffraction analysis of NIST fly ash standard reference materials. Powder Diffraction 15, 163-172 (2000).
8. Chancey, R. T., Stutzman, P., Juenger, M. C. & Fowler, D. W. Comprehensive phase characterization of crystalline and amorphous phases of a Class F fly ash. Cement and Concrete Research 40, 146-156 (2010).
9. Goldstein, J. et al. Scanning Electron Microscopy and X-ray Microanalysis (3rd ed.) (Springer Science + Business Media, New York, 2003).
10. Göetz, L. W., Göetz, G. &Sabbioni, E. Mobilization of heavy metals from fossil-fuelled power plants, potential ecological and biochemical implications: assessment studies of the European situation part4. EUR 6998, 1–165 (1981).
11. Bright, D. S & Newbury, D. E. Concentration histogram imaging. Analytical Chemistry 63, 243-250 (1991).

12. Newbury, D. E. et al. Compositional mapping with the electron probe Microanalyzer: Part II. ANALYTICAL CHEMISTRY 60, 1245-1254 (1990).
13. Fernández-Jiménez, A. &Palomo, A. Characterization of fly ashes. Potential reactivity as alkaline cements. Fuel 83, 2259-2265 (2003).
14. Li, C., Li, Y., Sun H. & Li, L. The Composition of Fly Ash Phase and Its Dissolution Properties Applying to Geopolymeric Materials. J. Am. Ceram. Soc. 94, 1773-1778 (2011).
15. Ward, C. R. & French, D. Determination of glass content and estimation of glass composition in fly ash using quantitative X-ray diffractometry. Fuel 85, 2268-2277 (2006).
16. Kutchko, B. G. & Kim, A. G. Fly ash characterization by SEM-EDS. Fuel 85, 2537-2544 (2006).
17. Rindby, A., Engström, P. &Janssens, K. The use of a scanning X-ray microprobe for simultaneous XRF/XRD studies of fly-ash particles. Journal of Synchrotron Radiation 4, 228-235 (1997).
18. Osan, J. of Solid Atmospheric Particles and the Environmental Cycle of Fly Ash (Semmelweis Medical University, Budapes, 1996).
19. Adams, F., Janssens K. &Snigirev, A. Microscopic X-ray fluorescence analysis and related methods with laboratory and synchrotron radiation sources: Plenary lecture. Journal of Analytical Atomic Spectrometry, 13, 319-331 (1998).
20. Kak, A. C. & Slaney, M. Principal of Computerized Tomographic Imaging (Society of Industrial and Applied Mathematics, Philadelphia, 2001).
21. Clackdoyle, R. &Defrise, M. Tomographic Reconstruction in the 21st Century. IEEE SIGNAL PROCESSING MAGAZINE, 60-80 (2010, July)
22. Kalender, W. A. Computed Tomography: Fundamentals, System Technology, Image quality, Applications (3rd ed.) (Publicis Publishing, Erlangen, 2011).
23. Alshibli, K. A. & Reed, A. H. Advances in Computed Tomography for Geomaterials: GeoX2010 (John Wiley & Sons, Inc, Hoboken, 2010).
24. Takeda, T. et al. X-ray fluorescent CT imaging of cerebral uptake of stable-iodine perfusion agent iodoamphetamine analog IMP in mice. Journal of Synchrotron Radiation 16, 57-62 (2009).

25. Winarski, R. P. et al. A hard X-ray nanoprobebeamline fornanoscale microscopy. Journal of Synchrotron Radiation 19, 1056-1060 (2012).
26. Provis, J. L., Rose, V., Winarski, R. P. & van Denventer, J. S. Hard X-ray nanotomography of amorphous aluminosilicate cements. ScriptaMaterialia 65, 316-319 (2011).
27. Rémond, S., Bentz, D.P., & Pimienta P. Effects of the incorporation of municipal solid waste incineration fly ash in cement pastes and mortars - II: Modeling. Cement and Concrete Research 32, 565-576 (2002).
28. Limaye, A. (2006). Drishti: Volume Exploration and Presentation Tool (Version 1.0.2) [Software], Available from http://anusf.anu.edu.au/Vizlab/drishti.
29. AMIRA (Version 4.1) [Software]. Burlington, MA: VSG.
30. Ritchie, N. (2008). DTSA II [software]. Retrieved from Public Domain. Software available from the NIST: http://www.cstl.nist.gov/div837/837.02/epq/dtsa2/index.html Gaithersburg, MD: National Institute of Standards and Technology.
31. Kotula, P.G., Keenan, M.R., Grant, R.P. &Hlava, P.F. Multivariable Statistical Analysis of Wavelength and Energy Dispersive X-ray Spectral Image. MicroscMicroanal 10, 118-119 (2004).
32. Exelis Visual Information Solutions. (2012). ENVI: Environment for Visualizing Images [software]. Software available from the Exelis Visual Information Solutions company: www.exelisvis.com.
33. Hubbell, J. H. Photon Mass Attenuation and Energy-Absorption Coefficients from 1 keV to 20 MeV. Int. J. Appl. Radiat. Isot. 33, 1269-1290 (1982).
34. ASTMC39,Standard Test Method for Compressive Strength of Cylindrical Concrete Specimens (ASTM International, Pennsylvania 2004).
35. ASTM C1293, Standard Test Method for Determination of Length Change of Concrete Due to Alkali-Silica Reaction (ASTM International, Pennsylvania 2004).
36. ASTM C1556,Standard Test Method for Determining the Apparent Chloride Diffusion Coefficient of Cementitious Mixtures by Bulk Diffusion (ASTM International, Pennsylvania 2004).